Noble Metal Nanoparticles

Supporting Tunable Fano Resonances for

Improving Plasmonic Solar Cells

A Thesis

Submitted to the Faculty

of

Drexel University

by

Bill Nguyen

in partial fulfillment of the

requirements for the degree

of

Master of Science in Materials Science and Engineering

January 2017

Dedications

Con cảm ơn bố mẹ đã luôn ủng hộ con và hy sinh cho con

Acknowledgments

First and foremost, I'd like to thank my family for their endless support and trust in me for whatever I pursue. For their support throughout my entire life whether I was only twenty miles from home or thousands of miles from home. Secondly, I'd like to thank all my friends, old and new, whom have pushed me when I needed motivation and picked me up when I have stumbled. Thank you for making me laugh when I've needed it and for listening to my complaints without protest.

I would also like to thank everyone that has been involved in my time abroad with the EAGLES program, which has been instrumental in molding my view of the world and molding myself into a person I am very happy to be.

I would like to thank the faculty at Drexel University in the Materials Science and Engineering (MS&E) Department as well as the Study Abroad Office for their help and flexibility with any question, no matter how small. A special thank you to my professors at Drexel and specifically my research advisor, Dr. Jonathan Spanier, for preparing me for the future. Another thanks for Marcia Henisz of the Study Abroad Office for always looking out for me and her pivotal role in shaping my excursion.

Vorrei ringraziare tutti coloro che ho incontrato in questa mia esperienza al Politecnico di Milano: i miei amici del gruppo DHAP, i miei docenti, che con passione mi hanno trasmesso la loro conoscenza ed infine la S.ra Michela Gregori dell'ufficio di Double Degrees. Grazie per aver condiviso con me le vostre culture, per avermi fatto sentire a casa a tanti chilometri di distanza, e ancora grazie per tutti i ricordi che siete riusciti a lasciarmi durante un anno pieno di cose belle. Sono sicuro che rivedró ancora questa città cosí come tutti voi. Milano e il tempo trascorso qui ci uniranno per sempre. Un ringraziamento speciale va, infine, al mio tutor di tesi del Polimi, Dott. Andrea Li Bassi, che con pazienza e dedizione mi ha aiutato a completare la mia tesi.

Finalmente, gracias a cada uno que conocí en Madrid y en la Universidad Politécnica de Madrid. En Madrid pase poco tiempo, sin embargo fue memorable. Gracias a mi "L'auberge Espagnole" por una calida bienvenida llena de comida, bebidas y música. Gracias a cada uno con los que trabajé en el Instituto de Fusión Nuclear (IFN) en UPM, por su amistad y por aceptarme en tan poco tiempo. Mi tesis no hubiera sido posible sin la ayuda de mi supervisor, el Dr. Ovidio Peña-Rodríguez, quién fue muy amable en ayudarme a completar la Tesis de Master en tan poco tiempo; fue quien leyó muchos borradores de mi tesis y fue extremadamente informativo, diligente, y amable.

Table of Contents

List of Tables

List of Figures

Abstract

Noble Metal Nanoparticles Supporting Tunable Fano Resonances for Improving Plasmonic Solar Cells
Bill Nguyen
Dr. Jonathan Spanier

Photovoltaic (PV) solar cell research is an increasingly growing field, largely due to the response to climate change. Many resources have been directed towards thin-film research specifically. Historically, thin-films have been held back by their inefficiency when absorbing and converting light. As a result, much thin-film research focuses on the improvement of absorbance efficiency. In particular, the use of nanoparticles supporting localized surface plasmon resonance (LSPR) in solar cells has been promising. The use of such plasmonic nanoparticles, termed "plasmonic solar cells" (PSCs), exploit the far field scattering and near electric field enhancement properties of nanoparticles in order to trap light and thus increase efficiency. These two key behaviors are strongest in the Fano resonance (FR) region of the spectrum.

In this work, we studied Fano resonance that appear on MDM gold-silica-gold nanoparticles in water using *scattnlay*, a computational Mie theory program. A variety of configurations of MDM nanoparticles were analyzed for their far field efficiencies, Fano resonance, scattering behavior, near field enhancement, and power flow.

Overall, results were found consistent with other studies. The Fano resonance occurs as a result of the interaction between the metal core and outer metal shell. The MDM nanoparticles were found to support Fano resonances for most cases, except for when the core-shell interaction was weak or when the core-shell energy modes did not spectrally overlap.

The Fano resonance affected the response of the nanoparticles to radiation. For the far field, the Fano resonance was found to create local minima and maxima in the asymmetry parameter spectrum that favored forward scattering. In the near field, the Fano resonance was found to

correspond to behaviors in the field enhancement. The FR center and maximum were found to correspond to the maximum field enhancement at the surface of the metal core and outer shell, respectively. In both cases, the MDM nanoparticles showed improvements over their monometallic counterparts. In addition, the presence of inward optical vortices was found to exist near the LSPR frequency.

It was concluded that a plasmonic solar cell configuration exploiting far field scattering properties would likely yield the best improvements; they exhibit preferential forward scattering in a high-scattering region. The MDM nanoparticles could be tuned to the full solar spectrum, scattering light forward and trapping light inside the solar cell.

Chapter 1: Introduction

1.1: Motivation

With the growing political and economic emphasis on climate change and energy independency, technological advancements of renewable energy sources are increasingly sought after. The issue with non-renewable resources, specifically fossil fuels, stems from their production of carbon dioxide, a greenhouse gas, as a by-product and their inability to replenish themselves. The main sources of renewable, clean energy are wind, water, and solar, each having their advantages and disadvantages. Solar energy, in particular, has a lot of promise but it is notoriously expensive due to the low efficiency attained so far in commercial solar cells and its high material costs. Hence, there is much technological progress to be made and abundant sunlight to be harnessed.

1.2: Solar Power

The sun, the ultimate source of energy of our planet, can be harnessed in multiple ways for its light and/or heat. Examples include solar heating, solar thermal energy, or solar fuel. Solar heating is commonly featured as a way to passively heat household pools. Solar thermal energy refers to using the heat instead to generate electricity, such as an array of mirrors heating water to spin an electric turbine. Solar fuel signifies the conversion of light/heat into chemical energy (for instance, by splitting water to generate hydrogen). However, the best known example for harnessing the sun's energy would be solar electricity via photovoltaics (PV), commonly seen in the form of solar cells.

The various types of photovoltaic solar cells are identified mainly by the semiconductor material they are manufactured from. Additionally, photovoltaic technologies have been categorized into three main "generations" (Figure 1.1). The first generation includes crystalline

silicon, in both single crystal and polycrystalline forms. The second generation is defined by thin-film solar cells. Finally, the third generation encompasses emerging technologies which aim to achieve high efficiency through a multiple energy-level structure [1].

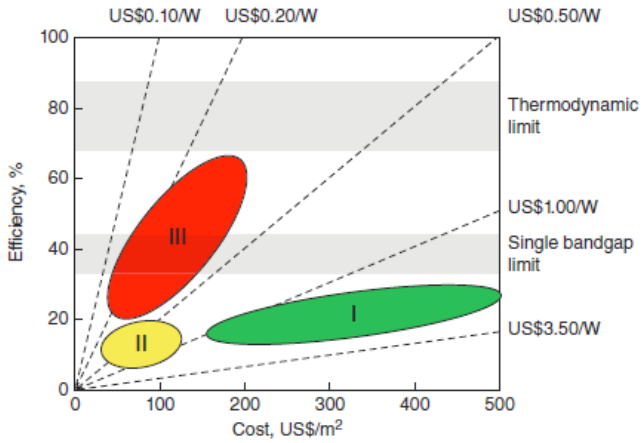

Figure 1.1: Solar cell efficiency vs. cost per unit area for three generations of solar cell technologies [1]

Currently and historically, first generation crystalline silicon technologies have dominated the market. Compared to second generation thin-film technologies, crystalline silicon has a complicated manufacturing process and higher cost. However, crystalline silicon has been able to remain dominant because of a high availability of silicon, a higher solar cell efficiency, and a longer lifespan (slower degradation) [2]. In addition, "silicon-based semiconductor fabrication is … a mature technology that enables cost-effective devices to be manufactured," largely in part due to the boom of the computer industry [3].

With all of the silicon's flaws, the solar cell industry was predicted to turn towards promising thin-film solar cells as a solution, given their favorable material properties. However, thin-film's percentage of commercial annual production has been shrinking against the more traditional crystalline silicon since 2009 (Figure 1.2). In 2015, thin-film solar cells made up less than 10% of the annual production versus the 90% of crystalline silicon.

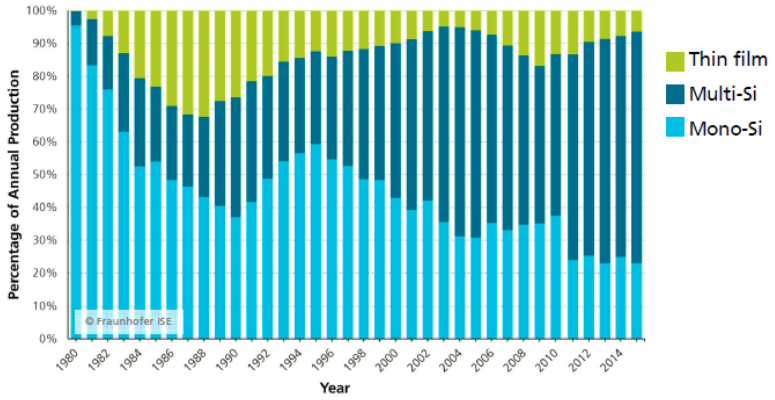

Figure 1.2: PV production by technology: percentage of global annual production over time for thin film and silicon technologies [4]

Unfortunately, thin-film solar cells are inherently limited by the same characteristics that make them promising. Thin-film solar cells are created by depositing a layer, on the order of microns, of a semiconductor onto a substrate. The probability of light being absorbed is proportional to the amount of material the light interacts with, which for thin-films would be very little. Increasing the thickness of the material, under current fabrication techniques would be extremely costly and difficult, while also taking away from the advantages thin-films can offer, such as flexibility of their substrates. Thus, one of the major limiting factors in the popularity of thin-film solar cells has been their ineffectiveness in absorbing near-bandgap light [5].

1.2.1: Plasmonic Solar Cells (PSCs)

Various schemes have been proposed to increase the absorption of light in thin-film solar cells. One particularly new and promising strategy is based on the use of subwavelength noble metal nanoparticles that exhibit a phenomenon known as localized surface plasmon resonance (LSPR). Hence, these type of solar cells have been dubbed as “plasmonic solar cells” (PSCs). Noble metal nanoparticles increase the photocurrent by two mechanisms: (1) when they are located on the top of the cell, they scatter the incident light into it and reduce the reflection and (2) embedded inside the absorber, they enhance the intensity of the absorbed light by concentrating the electric

field in their near field [5]. These two mechanisms occur strongest in the vicinity of where the LSPR takes place.

In a more general form, surface plasmons are collective oscillations, or density waves, of a metal's free electrons at the interface between negative permittivity (typically metallic) and positivity permittivity (dielectric) materials. Electrical permittivity is a measure of the ability to store and release energy from an electric field. The dielectric helps sustain the charge imbalance in the system, and thus, the wave.

Surface plasmons oscillate at a frequency much higher than the incident light, bypassing the classical limit (Rayleigh criterion) for the resolution of a lens (approximately a half-wavelength of incident light). This behavior, called surface plasmon resonance (SPR), occurs at the critical transparent frequency for the incident electromagnetic waves [6]. The critical transparent frequency is simply called the plasma frequency. "Surface" as opposed to, say, bulk, refers to the confinement of the plasma waves to the boundary between a metal and dielectric, in the form of exponentially decaying evanescent waves. When the plasma wave's electrons attempt to escape the surface, they travel shortly into the dielectric medium before ultimately being recaptured by the strong Coulomb attraction force caused by the charge imbalance caused by their absence.

Localized surface plasmon resonance occurs when SPR is limited to a nanoparticle or void on the magnitude of the wavelength. In the evanescent region, or near field, the LSPR magnifies the electric field significantly. It is worth noting that the frequency at which the LSPR occurs most strongly (the LSPR frequency) is different from the plasma frequency as predicted by the Drude model. In the far field, the location of the LSPR frequency is related to the maximum of the extinction of the beam [7]. The extinction of light by a particle is the sum of the light scattered plus the light absorbed [8]. The behaviors of the near field and far field depend on geometrical and electronic parameters. The combination of the two fields give metal nanoparticles useful optical properties. Noble metals, specifically gold (Au) and silver (Ag), are particularly well suited for plasmonics because their plasmon resonance occurs in the visible region of the light spectrum (400-

700 nm, 1.7-3 eV) while being chemically stable [7]. Note that other metals, like copper also fulfill these requirements but their LSPR frequency is located in the vicinity of their band gap, which damps their LSPR because the absorbed photons are used to promote electrons to the conduction band instead of exciting the LSPR.

In thin-film plasmonic solar cells, the optical properties of noble metal nanoparticles can be exploited using two main configurations. In the first configuration (Figure 1.3a), nanoparticles are located on the surface of the top dielectric spacer in order to both scatter and trap the light. Light scattered by a nanoparticle between two dielectrics will preferentially scatter into the dielectric material of higher permittivity [9], increasing the optical path. Moreover, light scattered at an angle greater than the critical angle (16° for a silicon-air) of the interface will stay trapped. In the second configuration (Figure 1.3b), the nanoparticles are located in between the dielectric spacer and absorber layer in order to act as antennas and lenses that locally focus light, thus increasing absorption efficiency of the semiconductor [10].

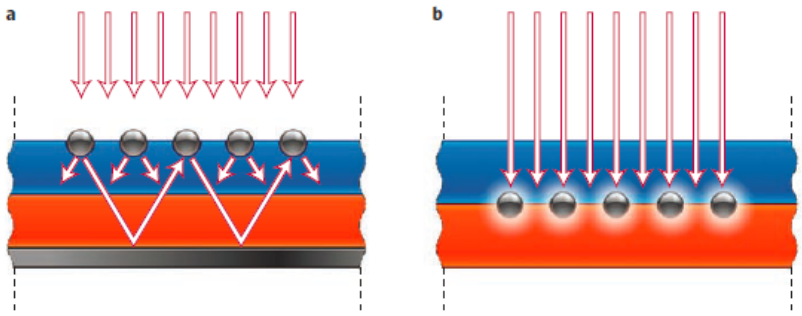

Figure 1.3: Thin-film plasmonic solar cell configurations. The top layer (blue) is the dielectric spacer. The bottom layer (orange) is the absorber layer. (a) The trapping of light by nanoparticles on the surface layer by scattering. (b) The trapping of light by localized surface plasmon resonance (LSPR) [10]

1.3: Fano Resonance (FR) and Plasmon Hybridization Theory

The region in which plasmonic nanoparticles exhibit their two key characteristics, far field extinction and near field enhancement, most strongly is in the Fano resonance. Fano resonances, first explained by Ugo Fano in 1961, are a type of resonance that manifests as an asymmetrical

line-shape, contrasting to, for example, a symmetrical Lorentzian peak (Figure 1.4) [11]. The Fano resonance itself is a general wave phenomenon that can occur in many different systems, such as classic, optical, or quantum. Resonant systems and signals were traditionally modelled as the superposition of different Lorentzian curves [12]. However, these models were unable to capture interference between the resonances. Fano resonance occurs as a result of the interference between a narrow mode and a continuum (or a wide mode) that overlap spatially and spectrally.

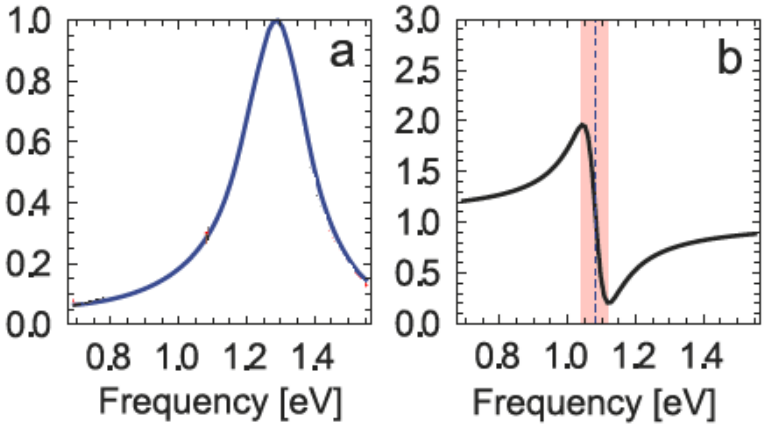

Figure 1.4: Comparison of (a) symmetrical Lorentzian and (b) asymmetrical Fano spectral line shapes of arbitrary experimental data [13]

In the case of symmetric nanoparticles, the wide energy mode is provided by scattering and the narrow mode is provided by absorption. The Fano resonance arises from the interaction between the two modes [13]. Individually, each line-shape is approximately Lorentzian, but interfere to give the asymmetric Fano resonance. Fano resonances in these multilayered symmetric nanoparticle systems, as well as those of more complicated geometries, have been explained previously using plasmon hybridization theory.

Plasmon hybridization theory explains more complicated structures by describing them as the interaction ("hybridization") of plasmons from simpler geometry. In turn, more and more complex shapes can be explained [14]. For example, the energy modes of a plasmonic nanoshell can be derived from a combination of a simpler sphere and cavity (Figure 5). The sphere and cavity

each have their own dipole energy modes. In the nanoshell, their dipole modes create two new "hybridized" plasmon energy modes. When the sphere/cavity modes are symmetric, it is a lower energy "bonding" mode ($|\omega_+\rangle$). When they are anti-symmetric, it is a higher energy "anti-bonding" mode ($|\omega_-\rangle$). The interaction and coupling strength between the mode of sphere and cavity in the nanoshell is determined by the geometric parameters, specifically the thickness of the ring.

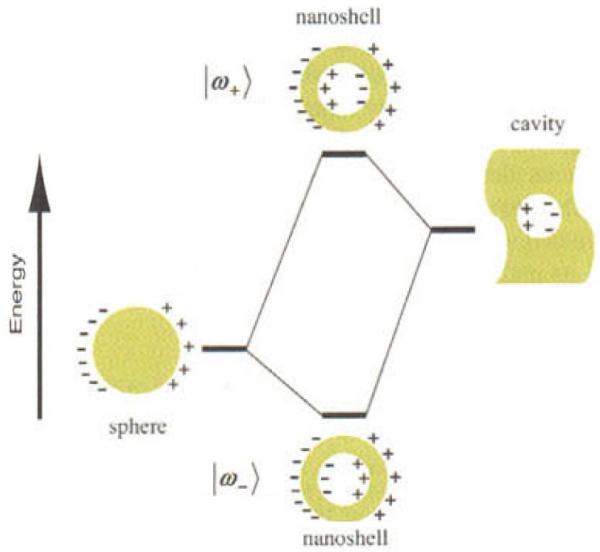

Figure 5: Energy diagram explaining plasmon hybridization in nanoshells as the interaction between a sphere and cavity. The interaction creates an asymmetric, higher energy mode (anti-bonding) and a symmetric, lower energy mode (bonding) [14].

In a similar logic, these nanoshells can be in turn be used to describe multilayered plasmonic nanoparticles (Figure 6). In short, the nanoshells again create a set of hybridized plasmonic modes. Such multilayered nanoparticles will be used and discussed in this work (Chapter 3.2). In particular, these nanoparticles are capable of exhibiting Fano resonances in their scattering spectrum. In these material systems, the Fano resonance conditions are provided by a super radiant, high energy dipolar antibonding mode (the wide mode) and a subradiant, low energy bonding mode (the narrow mode) that overlap in energy [12, 15, 16].

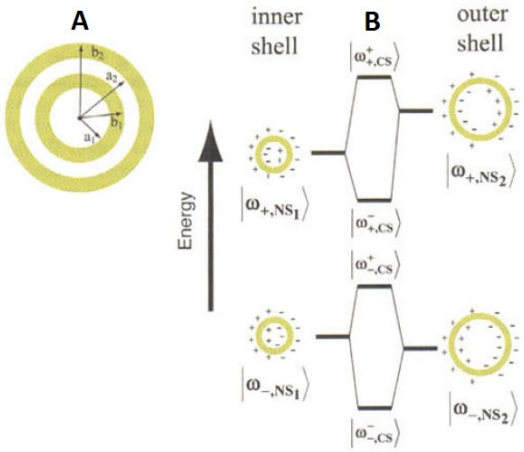

Figure 6: Energy diagram explaining plasmon hybridization in multilayered nanoparticles as the interaction between two nanoshells. In this system, four plasmonic hybridized energy modes are created [14].

Fano resonance supported by plasmonic nanoparticles also feature the ability of being "tuned". This predictable behavior allows for the optimization of the resonance intensity, as well as for adjusting the resonance spectrum into a favorable range (e.g. the air mass 1.5, or AM1.5, spectrum for which most solar cells are calibrated), a process called "tuning". The two major controllable factors for the spectral line shape and location are the material composition and geometric parameters. Finally, the line shape, intensity, and position of the far field behavior of nanoparticles can be calculated reliably using Mie Theory [17, 18].

1.4: Thesis Outline

In 1995, Stuart and Hall first used plasmonic nanoparticles on a silicon semiconductor to enhance absorbance of the infrared spectrum, to great effect [19]. Eventually, knowledge of the nanoparticle-semiconductor interaction for use in increasing absorbance entered the mainstream, but by 2008 there was still much progress to be made in the field of PSCs. One particular difficulty was predicting the behavior of nanoparticles embedded in the substrate in order to optimize design, particularly the balancing of nanoparticle properties in between two dielectric mediums [5, 10]. In short, the phenomenon was well-known, but not the underlying processes. By 2010, the researchers acknowledged the promise of PSCs and systematic studies of the material system mechanisms

began [10]. In present day, various research groups have used a variety of metal nanostructures in solar cells [20] and many mechanisms are better understood. However, to the best of the author's knowledge, an approach involving tuning nanoparticles has not been attempted. The theoretical foundations and tools for bottom-up PSC design have not always been readily and widely available. The use of a computational methods allows a deeper understanding of a variety of mechanisms in plasmonic systems. Hence, we will use *scattnlay*, to calculate the far and near field properties of multi-layered nanoparticles [18, 21], in order to find the best configurations to optimize the efficiency of PSCs with the help of these structures.

The improvement of thin-film plasmonic solar cells will increase the absorbance efficiency of already existing systems, or allow the reduction of thin-film thickness in newer systems. The reduction in semi-conductor thickness allows charge carriers to travel a shorter distance before creating a photocurrent, thus raising efficiency. Popular thin-film materials such as CdTe or $CuInSe_2$ are vulnerable to supply-chain problems, so using less material can alleviate some demand. The configuration can be readily applied to other semiconducting materials, allowing for a greater variety of materials to be feasible [10]. Improving thin-film solar cells could help move out of their currently niche applications.

In the wider scope, the research of plasmonic mechanisms alone will prove useful. Plasmonic nanoparticles have uses in a variety of fields, including, but not limited to biology, chemistry, and physics [22]. One of the quickest commercial adaptions of surface plasmon resonance (SPR) has been in the field of biosensing. In most SPR biosensing instruments, a detector monitors a nanoparticle surface in real-time. A molecular interaction, such as an antibody and antigen, causes a shift in the LSPR peak [23]. Plasmonic mechanisms have also been exploited in microscopy to overcome the classical resolution limit. The resolution of, for example, an optical microscope is limited to about half the wavelength of the light shining on the surface [6]. Surface plasmons resonate at a frequency much greater than the incident light, allowing them to resolve much smaller features. Therefore, in the near field, a higher resolution can be achieved [24]. Finally,

plasmonic materials are a trending topic on the forefront of research. Explorative research has tried to apply plasmonics for use in light emitting diodes by exploiting the nanoparticles as sub-wavelength antennas to increase conversion efficiency [25].

In summary, this work will study the optical properties of tunable, noble metal nanoparticles in the far and near field. The software chosen, *scattnlay* [18], is based off of Mie theory, for which analytical, exact expressions for scattering and absorption cross sections can be calculated. The ultimate goal of the work is to optimize the properties for use in plasmonic solar cells. Although thin-films solar cells are cheaper to manufacture, their inefficient absorption has caused many setbacks in their popularity. Much research and effort has been placed into overcoming an inherent flaw. In particular, plasmonic multilayered spherical noble metal nanoparticles can be used to increase absorbance efficiencies by exploiting their far field scattering and near field enhancement properties. Such particles are relatively easy to manufacture, exhibit tunable Fano resonances in the visible light range, and can be tuned for specialized use. Reliable calculations of nanoparticle behavior allow software to play an instrumental role in leading a low-cost design phase for plasmonic nanoparticles and a deeper understanding of the system mechanisms.

Chapter 2: Background and Theory

2.1: Solar Cells

Solar cells utilize the photovoltaic effect to generate electricity from solar radiation. The photovoltaic effect, first reported and discovered by Becquerel in 1863, is the phenomenon by which electricity is generated by electromagnetic radiation upon striking a material system [2]. The conversion of sunlight into usable energy in individual photovoltaic cells depends on two fundamental steps. First, light must be absorbed to create an electron-hole pair, also known as an exciton. Next, the structure of the device must separate the oppositely charged carriers to avoid recombination, creating a potential difference, and thus, an electric current [26]. Usually, several solar cells will be assembled together to create a larger module, or "solar panel", capable of generating practical amounts of electricity.

By far, silicon is the most popular solar cell semiconductor material, despite having numerous drawbacks. From a solid state physics perspective, it is a poor absorptive semiconductor. The sun's solar spectrum, as estimated by a black-body, ranges from near-infrared to ultraviolet (Figure 2.1). Single band semiconductors are limited in the efficiency in which they can absorb incident photons. Photons at a lower energy (longer wavelength) than the semiconductor bandgap energy will see the material as transparent, or pass through without being absorbed. Meanwhile, photons at a higher energy (shorter wavelength) than the bandgap energy will see be absorbed (opaque) but also lose energy as heat in order to match the exact bandgap energy. In this perspective, silicon, at a bandgap of 1.11 eV is not optimal when compared to Gallium Arsenide (GaAs, bandgap of 1.42 eV) on an efficiency vs. bandgap energy chart (Figure 2.2) [6].

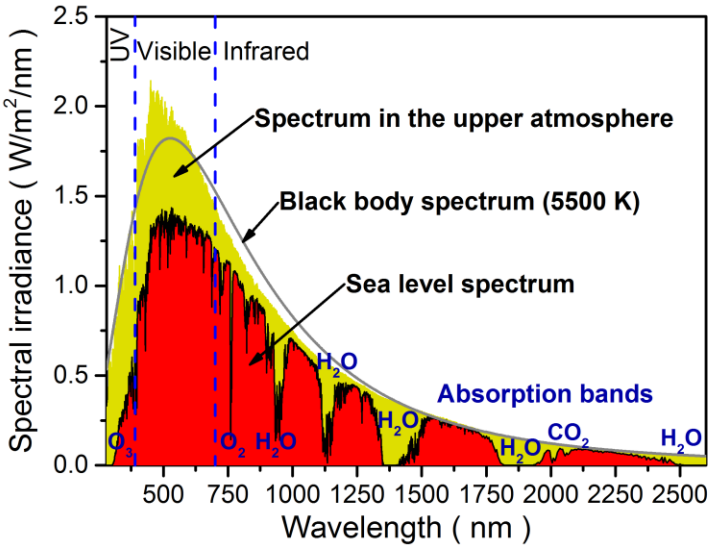

Figure 2.1: Solar spectrum of the sun

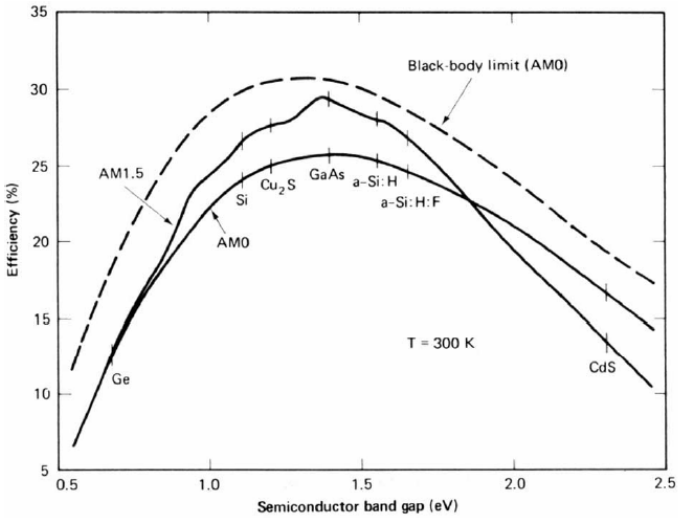

Figure 2.2: Conversion efficiencies of various semiconductors versus their bandgap energies [2]

However, the largest shortcoming of silicon is its status as an indirect semiconductor as opposed to a direct semiconductor. Absorption depends on the underlying mechanisms of the material system. Firstly, the density of states available for electrons to occupy must exist, both in the valence band to the conduction band of the electronic structure. Thus, the absorption depends on the density of states both in the valence band and conduction band. Secondly, the quantum mechanical transition between bands must conserve both energy *and* momentum [3]. The quantum

analog to momentum is proportional to the wave vector, k. The visualization of direct and indirect band structures is best represented by an energy-wave vector ($E - k$) curve (Figure 2.3).

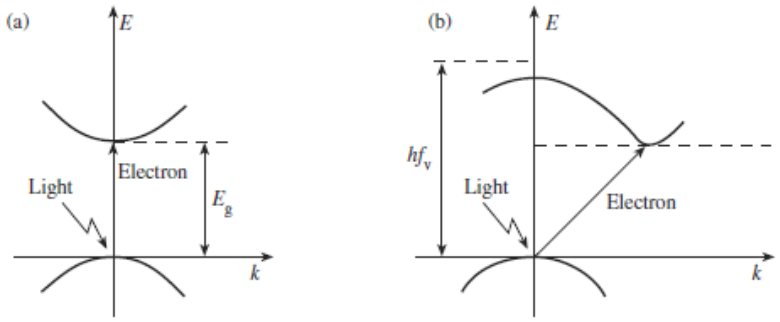

Figure 2.3: $E - k$ curves for (a) direct and (b) indirect semiconductors upon photon absorption [6]

For a direct bandgap semiconductor (Figure 2.3a), the incident photon excites an electron directly from the valence to the conduction band. In other words, only having sufficient energy is enough in this scenario. Meanwhile, for an indirect bandgap semiconductor (Figure 2.3b), the maximum of the valence band and minimum of the conduction band are offset by a certain momentum. Meaning that there must be a certain energy *and* momentum in order to make the transition. The insufficiency of momentum by the excited electron is compensated by the lattice phonons, which, at a given frequency (energy), will have a momentum several orders magnitude larger [6]. This three-particle process, photon-electron-phonon, is less likely to occur than the two-particle process of direct bandgap semiconductors, thus indirect bandgap semiconductors like silicon are much less efficient.

Accordingly, much more silicon must be used in order to achieve the same absorption as a direct bandgap material such as GaAs. To achieve "90% light absorption it takes only 1 μm of GaAs versus 100 μm of Si" [2]. The large discrepancy in required thicknesses is how thin-films received their name. Additionally, the charge carriers must have the diffusion properties necessary to reach the front and back contacts of the solar cell (about twice the thickness of the cell). The

material is required to be of high quality, in terms of purity (low presence of other elements) and crystallinity (as close to single crystal as possible). In fact, the requirement for light absorption and small thickness compete with one another [10].

Material selection and properties are paramount to solar cell design. There are several requirements for the optimal solar cell material. In terms of the electronic structure, the material's bandgap must be in the range of visible light (1.7-3 eV), the bandgap should be direct, and the material must have good absorption and photovoltaic efficiency. In the sense of manufacturing, the material must be abundant, non-toxic, low degradation, and capable of large scale production [2]

Solar cell design faces two main fundamental limits. The Shockley-Quiesser limit [27] for single p-n junction solar cells is the first. The limit for a concentration of one sun is about 31% and for 1000 suns is about 37%. The Shockley-Quiesser limit can be overcome by using multi-junction solar cells, or those with a range of bandgap values. For multi-junction solar cells, thermodynamics imposes the second set of limits. For a concentration of one sun, the lower value is about 72%. For a concentration of 1000 suns the idealistic, upper value is about 93% [26, 28].

2.2: Light Scattering

Because all matter is made of protons and electrons, light incident on a particle will interact with its discrete charges, in the form of coupling. The coupling causes an oscillatory acceleration motion, manifesting as a dipole moment. The acceleration itself causes a secondary radiation, different from the incident beam, that scatters in all directions. In short, scattering is the result of a particle's excitation by an incident electromagnetic wave, and then the reradiation of that energy. Reradiating energy is not the only outlet for the particle. The excess energy can be transformed into a different form, like heat—a process that is called absorption [8].

Despite scattering phenomena ultimately occurring as a result of the response of discrete particles, there are laws and formulas dictating the average, macroscopic behavior for different

media. The most famous such example would be the empirically derived Snell's law. One form of Snell's law can be seen in (2.1), where the subscripts 1 and 2 represent different media. Equation (2.1) simply states that the ratio of the angle of the incident beam to the refracted beam is proportional to the ratio of the refractive indices (albeit in reverse).

$$\frac{sin(\theta_1)}{sin(\theta_2)} = \frac{n_2}{n_1} \tag{2.1}$$

Physically, the refractive index is a value that captures the average behavior of all the molecules upon which the light is incident. The particles respond to two different electromagnetic fields: the primary electromagnetic field of the incident light, and the secondary field caused by scattering. The secondary field can be difficult to calculate; it is produced by particles, whose behavior, again, is dependent on the secondary fields themselves. Despite this, in the far field region, the secondary, scattered waves superpose and follow an average behavior captured by the refractive index. The original, incident beam is considered to extinguish completely (Ewald-Oseen extinction theorem) and instead produces two waves: the reflected wave and refracted wave. The reflected and refracted beams are a direct result from the superposition of secondary waves. In fact, the refractive index depends on the number density of the particles and the polarizability of each [8].

Conveniently, the induced dipole moment for a single particle at a given frequency is related to the bulk behavior. In general, the secondary scattering will depend on the angle of the scattering and the size of the particle. For particles much smaller than the wavelength the secondary waves will be in phase. However, as the size increases, there is a greater chance of constructive and destructive peaks. The relationships of the constructive/destructive relations of the waves being in/out-of-phase depends on a variety of geometric factors [8].

It is worth noting that light scatters in all directions and that Snell's law approximates the first-order, or strongest, behavior. Snell's law also works under many assumptions that are true for most materials, as long as they are optically dense and statistically homogeneous. Essentially, it is necessary that the interatomic spacing and their statistical fluctuations be negligible with respect to the size of visible light. Finally, the frequency of the wave is a constant, acting as a boundary condition at the interface [8].

2.2.1: Far Field Light Scattering by Particles

Although scattering phenomena are wide in scope, the behavior of most can be captured in a general model. Consider a polarized, monochromatic wave shining on a particle of arbitrary geometry and optical properties in a homogeneous medium. The resulting electromagnetic field can be determined for all points inside the particle and outside in the medium. The electromagnetic field of the medium is given by the superposition of the incident and scattered fields. All fields are also waves which must obey Maxwell's equations (2.2-5) for which permittivity (ε) and permeability (μ) are continuous [8]. Indeed, solving the electromagnetic field equations inside and outside the particle will describe the behavior.

$$\nabla \cdot \boldsymbol{E} = 0 \tag{2.2}$$

$$\nabla \cdot \boldsymbol{H} = 0 \tag{2.3}$$

$$\nabla \times \boldsymbol{E} = i\omega\mu\boldsymbol{H} \tag{2.4}$$

$$\nabla \times \boldsymbol{H} = -i\omega\varepsilon\boldsymbol{E} \tag{2.5}$$

With the solved EM equations, the Poynting vector can be determined at any point. The Poynting vector "specifies magnitude and direction of rate of transfer of electromagnetic energy at

all points in space," which is useful in studying far field interactions. The time-averaged Poynting vector is determined from not only the incident and scattering fields, but also their interaction:

$$\boldsymbol{S} = \frac{1}{2} Re\{\boldsymbol{E} \times \boldsymbol{H}^{\star}\} = \boldsymbol{S}_i + \boldsymbol{S}_s + \boldsymbol{S}_{int} \tag{2.6}$$

The time-averaged Poynting vector is usually calculated as the real parts of product between the electric field ($\boldsymbol{E}$) and the complex conjugate of the magnetic field ($\boldsymbol{H}^{\star}$). In the case of the particle, the time-average Poynting vector for any space in the medium is the sum of Poynting vectors of the incident, scattering, and interaction terms.

The polarization of light can be described by a four-component vector called the Stokes vector (2.7). In the problem of light scattered by a small particle, the Stokes vectors of the scattered light is related directly to the incident stokes vector (2.8), where $\hat{S}$ is the amplitude scattering matrix (2.9) [18].

$$\hat{I} = [I, Q, U, V]^T \tag{2.7}$$

$$\hat{I}_s \propto \hat{S}\hat{I}_i \tag{2.8}$$

$$\hat{S}(\theta) = \begin{bmatrix} S_{11}(\theta) & S_{12}(\theta) & 0 & 0 \\ S_{21}(\theta) & S_{11}(\theta) & 0 & 0 \\ 0 & 0 & S_{33}(\theta) & S_{34}(\theta) \\ 0 & 0 & -S_{34}(\theta) & S_{33}(\theta) \end{bmatrix} \tag{2.9}$$

Where θ is the scattering angle, or angle between the direction of the incident and scattered radiation. The elements of the scattering matrix can be calculated from the scattering amplitudes $S_1(\theta),\ S_2(\theta)$ as [18]:

$$S_{11}(\theta) = \frac{1}{2}[|S_2(\theta)|^2 + |S_1(\theta)|^2] \tag{2.10}$$

$$S_{12}(\theta) = \frac{1}{2}[|S_2(\theta)|^2 - |S_1(\theta)|^2] \tag{2.11}$$

$$S_{33}(\theta) = [S_1(\theta)S_2^\star(\theta) + S_1^\star(\theta)S_2(\theta)] \tag{2.12}$$

$$S_{34}(\theta) = [S_1(\theta)S_2^\star(\theta) - S_1^\star(\theta)S_2(\theta)] \tag{2.13}$$

The convenience of the amplitude scattering matrix is that the behavior of many particles can be given by the sum of their amplitude scattering matrices. Essentially, the complicated behavior can be more easily modeled by using the sum of their parts [8].

Scattering (including absorption) by a particle can be captured quantitatively. Matter, and its discrete charges, interacting with radiation through coupling will cause a certain loss of energy. The loss of strength of the beam, called "extinction", is composed of the energy loss due to both absorption and scattering by the particles. The energy loss due to extinction can be described by the extinction cross-section (2.14), which is the ratio of the loss of energy to the intensity of the incident beam. Scattering (2.15) and absorption counterparts for the extinction cross-section exist. The relationship between the three cross-sections are given by (2.16) [8]. The quantity $|X|^2/k^2$ used in the definition of (2.15) is the "differential scattering cross-section", representing the amount of light per unit angle in a direction.

$$C_{ext} = \frac{W_{ext}}{I_i} \tag{2.14}$$

$$C_{sca} = \int_{4\pi} \frac{|X|^2}{k^2} d\Omega \tag{2.15}$$

$$C_{ext} = C_{abs} + C_{sca} \tag{2.16}$$

The nomenclature of "cross-section" comes from the terms having the units of area. The extinction cross-section can be given some physical significance by looking at a scenario between

light shining on a detector with a particle in the center. From the perspective of the detector, the cross-section is the amount of light the particle blocks from the detector creating a dark spot, or "shadow", on the surface, is related to the extinction cross-section [8]. From the perspective of light, the extinction cross-section is the size of the particle that the light "sees". However, the apparent size of the particle from the point of view of the light or the detector is not only related to its size but also its optical properties.

All of the cross-sections have dimensionless counterparts, also called efficiency factors. The efficiency factors are given by dividing the dimensional cross-sections by G, the projection of the shape of the particle onto a plane (2.17a,b,c) [8]. Note that the efficiency factors can take values greater than one.

$$Q_{ext} = \frac{C_{ext}}{G}, Q_{sca} = \frac{C_{sca}}{G}, Q_{abs} = \frac{C_{abs}}{G} \tag{2.17a,b,c}$$

The reduced differential scattering cross-section can be calculated with the help of the scattering amplitudes and scattering matrix (2.18). The *reduced* differential scattering cross-section serves the same purpose of the efficiency factors, in that it allows comparison between particles. $S_{11}(\theta)$ is the element in the scattering matrix previously defined in (2.10) and $k = 2\pi n_m/\lambda$ where n_m is the refractive index of the host medium and λ is the wavelength of incident light in vacuum.

$$\frac{dC_{sca}}{d(a^2\Omega)} = \frac{S_{11}(\theta)}{k^2} \tag{2.18}$$

2.2.2: Mie theory

Analytical, exact expressions for far field scattering and absorption cross sections can be derived from Mie theory. The original Mie formulation was for a spherical particle embedded in a

homogenous medium. Mie theory relies on solving Maxwell's equations in spherical polar coordinates, taking advantage of system symmetry [29]. Gustav Mie, to whom Mie theory is credited, simplified the mathematics of the problem by reducing the governing field equations to scalar wave equations [8]. Since its conception, Mie theory has been expanded for more complex problems, including multilayered spheres [16, 17]. The details of Mie theory, including its implementation in the chosen computational code, *scattnlay* will be discussed in Chapter 3.

2.3: Fano Resonance (FR) of Plasmonic Nanoparticles

The Fano resonance (FR) of metal-dielectric-metal (MDM) plasmonic nanoparticles can be estimated at a first approximation by subtracting the scattering cross-section, Q_{sca}, spectrum of the MDM nanoparticle with an equivalent system where the metal core is replaced entirely by the dielectric (a dielectric-metal nanoparticle). This is because the Fano resonance in MDM system occurs as a result of the coupling interaction between the metal core and the outer metal shell. The center of the Fano spectrum can be approximated as the maximum of the absorption cross-section, Q_{abs}, spectrum.

However, the first approximation will tend to fail as the coupling effect becomes weaker. These edge conditions will be met when one layer of the shell is much smaller or bigger than the others. In these cases, a line fit to for the Fano spectrum must be used [16]. An equation for the line shape of plasmonic Fano resonances from Gallinet and Martin will be used [13]. In their framework the resonance strength of the system is a convolution in the form of a product between a symmetric pseudo-Lorentzian (2.19) peak and an asymmetric Fano (2.20) curve. Upon spatial and spectral overlap, their product manifests in the form of the observed scattering cross-section, Q_{sca} (2.21).

$$\sigma_s(E) = \frac{a^2}{\left(\frac{E^2 - E_s^2}{2E_s\Gamma_s}\right)^2 + 1} \tag{2.19}$$

$$\sigma_a(E) = \frac{\left(\frac{E^2 - E_a^2}{2E_a\Gamma_a} + q\right)^2 + b}{\left(\frac{E^2 - E_a^2}{2E_a\Gamma_a}\right)^2 + 1} \tag{2.20}$$

$$\sigma_t(E) = \sigma_s(E) \cdot \sigma_a(E) = Q_{sca}(E) \tag{2.21}$$

The subscripts s and a refer to the symmetric Lorentzian and asymmetric Fano curves. For the Lorentzian resonance peak of (2.19), the variable a is the maximum amplitude, E_s is the resonance energy position, and Γ_s is the approximate spectral width. Likewise, for the Fano resonance peak of (2.20), the variable q is the Fano asymmetry parameter, b is the modulation damping parameter, E_a is the resonance energy position, and Γ_a is the approximate spectral width. All of the equations are a function of energy, E.

Additionally, a sigmoidal term (2.22) can be defined in order to subtract out background radiation in the interband absorption of gold where $B_1, A_1, A_2,$ and E_0 are the offset amplitude, slope and position of the sigmoid with values of -1.66, 2.21, 2.84 eV^{-1}, and 2.5 eV^{-1}, respectively [16].

$$B_1 + \frac{A_1}{1 + exp\left(-A_2 \cdot (E - E_0)\right)} \tag{2.22}$$

The Fano resonance behavior in MDM systems cannot be observed immediately. Instead, changes in the Fano resonance will surface in the changing line shape of σ_t. The four parameters specific to the Fano resonance curve are the asymmetry parameter (q), the modulation damping parameter (b), the Fano position (E_a), and the Fano spectral width (Γ_a). The asymmetry parameter roughly translates as how the peak and the valley of the Fano resonance will be (Figure 1.4b). Its effect on σ_t when all other line fitting parameters are held constant can be seen in Figure 2.4. The Lorentzian resonance and the Fano center, which are constant, are provided as a reference.

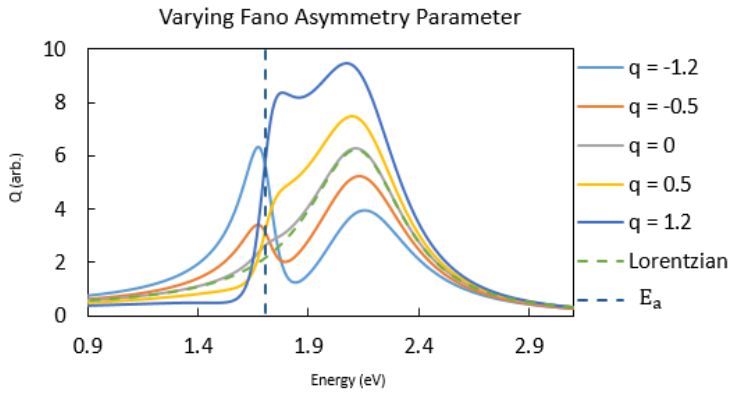

Figure 2.4: Varying Fano asymmetry parameter, with all other parameters held constant

At low q, there is strong evidence of the Fano resonance interacting with the Lorentzian peak. At this large, negative value, the maximum of the Fano resonance is on the left, while the minimum is on the right, close in spectrum to the Lorentzian position. When q increases, but is still negative, both peaks are seen, but the multiplication between the Lorentzian and Fano minimum causes the rightside peak to become the absolute max. At $q = 0$, the Fano resonance has little effect on the overall spectrum, with σ_t having nearly an identical line shape to the Lorentzian resonance, apart from the area in the vicinity of the Fano. When q turns positive, the maximum and minimum of the FR have switched relative positions (left-right). The Lorentzian curve, whose position is constant, now constructively interferes with the new Fano maximum and its magnitude becomes greatly exaggerated.

The parameter b "quantifies the modulation damping of the resonance by intrinsic losses" [13]. Essentially, it will control the magnitude and sharpness of the minimum/maximum peaks of the Fano resonance. The effects of the modulation damping parameter on σ_t can be seen in Figure 2.5.

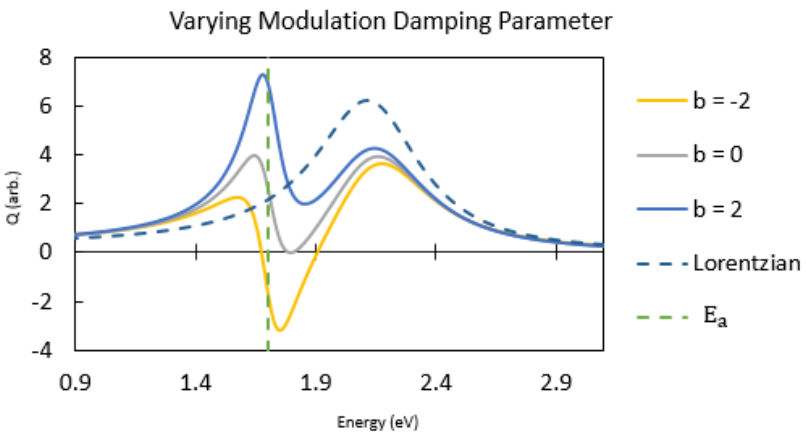

Figure 2.5: Varying modulation damping parameter, with all other parameters held constant

Regardless of the value of the damping parameter, one sees two peaks in the spectrum because of the chosen values for the asymmetry, q, and the difference in the positions of the Fano and the Lorentzian peaks. In this problem, Fano resonance is centered (E_a) at a lower energy in the spectrum with its maximum on the left and minimum on the right. At a negative value of $b = -2$, the Fano resonance minimum is more negative, causing a deeper minimum in σ_t. With no damping, i.e. $b = 0$, the Fano still skews the curve, causing two peaks, but not as extreme as the other cases. Finally, at positive values, such as $b = 2$, the maximum of the Fano resonance is instead exaggerated. In this case, the high b value causes the left peak in the σ_t spectrum to become the absolute maxima over the right peak.

The observed behavior is also dependent on the position of the Fano resonance relative to the Lorentzian resonance. Depending on where the two resonances overlap, the relative extrema can interfere constructively or destructively with the Lorentzian resonance. The position of the Fano resonance (E_a) below, equal, and above the Lorentzian position (E_s) can be seen below in Figure 2.6. For the parameters in this problem, the maximum of the Fano will be observed on the left-hand side and its minimum on the right-hand side of its center.

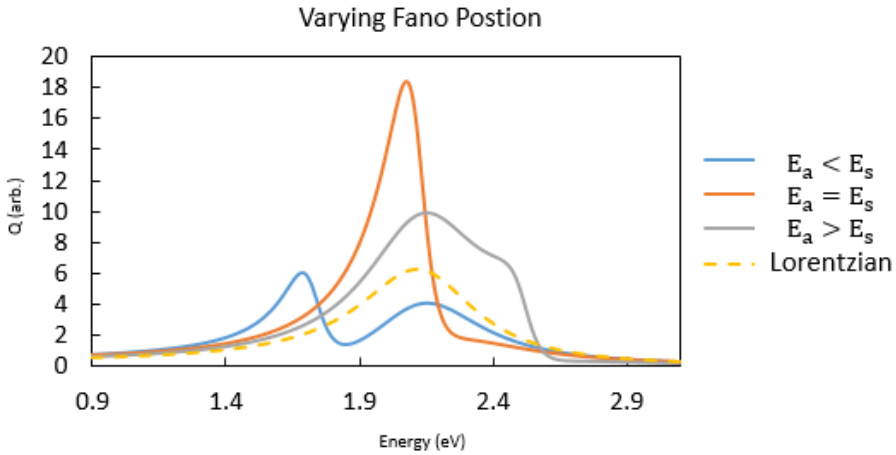

Figure 2.6: Varying Fano position relative to Lorentzian. Note that x-axis is in nanometers, not energy

When the Fano resonance is red-shifted ($E_a < E_s$), the peak related to the Lorentzian has been suppressed and the Fano maximum protrudes. When the center of the Fano coincides with the Lorentzian ($E_a = E_s$), the proximity of the Fano maximum to the Lorentzian peak causes them to multiply together to produce an extremely sharp, strong peak. The sharpness is further exaggerated because the minimum of the Fano has "lowered" the right-hand side of the spectrum. Finally, when the Fano resonance is blue-shifted ($E_a > E_s$), the maximum of the Fano does not match as well with the Lorentzian, producing a relatively milder, but broader peak.

In this work, the Fano resonance will be unable to be measured directly. Instead, behavior will be immediately observed by viewing the far field scattering spectrum, Q_{abs}, from which a good, initial understanding of the underlying behaviors can be inferred before performing the line fitting procedure to study the Fano resonance directly.

Chapter 3: Method and Materials

The use of software for optimizing the nanoparticles for use in solar cells allows a lower cost during the design phase. The nanoparticles studied in this work will have a configuration, metal-dielectric-metal (MDM), where the outer layer and the inner core are noble metals (usually Au or Ag), separated by a dielectric layer. The properties of multilayered, noble metal nanoparticles will be calculated using s*cattnlay*, capable of calculating near field and far field behavior using Mie theory [18]. *Scattnlay* will be interfaced by means of the programming language *Python 2.7* [30].

3.1: Mie Theory and *scattnlay* (Solid Sphere)

The original work of Mie solved Maxwell's equations for a solid metal sphere in a homogeneous medium, impinged on by an electric field that is a plane, x-polarized wave, $\boldsymbol{E}_i = E_0 \exp(ikr \cdot cos(\theta)\boldsymbol{e_x})$, with a time dependence of $\exp(-i\omega t)$. The sphere is characterized by a size parameter, x (3.1), and a relative refractive index, m (3.2):

$$x = k \cdot r = \frac{2\pi n_m r}{\lambda} \tag{3.1}$$

$$m = \frac{n_p}{n_m} \tag{3.2}$$

where k is the wave number in the dielectric medium, r is the radius, λ is the wavelength of the incident light in vacuum, and n_p and n_m are the refractive indices of the sphere and host medium, respectively. The computational goal of Mie theory is to calculate the scattering coefficients:

$$a_n = \frac{\left(m\psi_n(mx)\psi_n'(x) - \psi_n'(mx)\psi_n(x)\right)}{\left(m\psi_n(mx)\xi_n'(x) - \psi_n'(mx)\xi_n(x)\right)} \tag{3.3}$$

$$b_n = \frac{\left(\psi_n(mx)\psi_n'(x) - m\psi_n'(mx)\psi_n(x)\right)}{\left(\psi_n(mx)\xi_n'(x) - m\psi_n'(mx)\xi_n(x)\right)} \tag{3.4}$$

Where ψ_n and ξ_n are the Riccati-Bessel functions, which are forms of the spherical Bessel and Hankel functions, respectively.

The scattering coefficients are used to calculate the far field behavior, best represented as cross sections:

$$C_{ext} = \frac{2\pi}{k^2}\sum_{n=1}^{\infty}(2n+1)\cdot Re\{a_n + b_n\} \tag{3.5}$$

$$C_{sca} = \frac{2\pi}{k^2}\sum_{n=1}^{\infty}(2n+1)\cdot(|a_n|^2 + |b_n|^2) \tag{3.6}$$

$$C_{abs} = C_{ext} - C_{sca} \tag{3.7}$$

3.1.1: Multilayered Sphere (Far Field)

Mie theory can be, and has been, extended for multilayered spheres [17]. In this case, the size parameter and refractive index are defined for each layer, $l = 1 \ldots L$

$$x_l = k \cdot r_l = \frac{2\pi n_m r_l}{\lambda} \tag{3.8}$$

$$m_l = \frac{n_l}{n_m} \tag{3.9}$$

The system is separated into two regions: one outside of the sphere (the medium) and another inside the sphere. The electromagnetic fields in both regions are represented as the superposition of inward and outward waves:

$$E_{inw} = \sum_{n=1}^{\infty} E_n[c_n^l M_{o1n}^1 - id_n^l N_{e1n}^1] \tag{3.10}$$

$$E_{outw} = \sum_{n=1}^{\infty} E_n[ia_n^l N_{e1n}^3 - b_n^l M_{o1n}^3] \tag{3.11}$$

which are in the form of complex spherical eigenvectors, where $E_n = i^n E_0(2n+1)/n(n+1)$ and $M_{o1n}^j \; and \; N_{e1n}^j$ $(j = 1,3)$, are the vector harmonic functions of the Bessel and Hankel functions [17]. Outside the sphere, the electromagnetic field is the superposition of the incident scattered fields, i.e. $E_{out} = E_i + E_s$ where:

$$E_i = \sum_{n=1}^{\infty} E_n[M_{o1n}^1 - iN_{e1n}^1] \tag{3.12}$$

$$E_s = \sum_{n=1}^{\infty} E_n[ia_n N_{e1n}^3 - b_n M_{o1n}^3] \tag{3.13}$$

In (3.10-13), the electromagnetic fields are expressed as series weighted by expansion coefficients $(a_n^l, b_n^l, c_n^l, d_n^l)$ and scattering coefficients (a_n, b_n). One can deduce that the expansion coefficients: $a_n^1 = b_n^1 = 0$ and $c_n^{L+1} = d_n^{L+1} = 1$ [17, 18]. By matching the tangent components of the electromagnetic fields at each interface the expansion coefficients and scattering coefficients can be obtained. The final expansion coefficients are related to the scattering coefficients:

$$a_n = a_n^{L+1} = \frac{\left[\frac{H_n^a(m_{Lx_L})}{m_L} + \frac{n}{x_L}\right]\psi_n(x_L) - \psi_{n-1}(x_L)}{\left[\frac{H_n^a(m_{Lx_L})}{m_L} + \frac{n}{x_L}\right]\zeta_n(x_L) - \zeta_{n-1}(x_L)} \tag{3.14}$$

$$b_n = b_n^{L+1} = \frac{\left[m_L H_n^b(m_L x_L) + \frac{n}{x_L}\right]\psi_n(x_L) - \psi_{n-1}(x_L)}{\left[m_L H_n^b(m_L x_L) + \frac{n}{x_L}\right]\zeta_n(x_L) - \zeta_{n-1}(x_L)} \tag{3.15}$$

where ψ_n and ζ_n are the Riccati-Bessel functions and H_n^a and H_n^b are calculated determinants of various expressions [17].

3.1.2: Multilayered Sphere (Near Field)

Calculations of the near field in a multilayered particle are also possible [21]. The framework for the region outside the particle are nearly identical. The electromagnetic field inside the particle can be represented as an expansion for each layer, l:

$$E_l = \sum_{n=1}^{\infty} E_n[c_n^l M_{o1n}^1 - id_n^l N_{e1n}^1 + ia_n^l N_{e1n}^3 - b_n^l M_{o1n}^3] \tag{3.16}$$

$$H_l = \frac{k_l}{\omega\mu}\sum_{n=1}^{\infty} E_n[d_n^l M_{e1n}^1 + ic_n^l N_{o1n}^1 - ib_n^l N_{o1n}^3 - a_n^l M_{e1n}^3] \tag{3.17}$$

Again, the electromagnetic fields are expressed as series weighted by expansion coefficients. The algorithm to solve (3.16-17) begins by calculating the scattering coefficients a_n and b_n, which are the expansion coefficients in the outer medium: $a_n = a_n^{L+1}$ and $b_n = b_n^{L+1}$. Then, expansion coefficients for the inner layers, a_n^l and b_n^l, can be calculated by a downward recurrence, using the following expressions (obtained by solving a set of linear equations that ensure the continuity of the fields at the interfaces) for the four expansion coefficients:

$$a_n^l = \frac{D_n^1(m_l x_l)T_1(m_{l+1}x_l) + T_3(m_{l+1}x_l)m_l/m_{l+1}}{\zeta_n(m_l x_l)\left(D_n^l(m_l x_l) - D_n^3(m_l x_l)\right)} \tag{3.18}$$

$$b_n^l = \frac{D_n^1(m_l x_l)T_2(m_{l+1}x_l)m_l/m_{l+1} + T_4\left(m_{(l+1)}x_l\right)}{\zeta_n(m_l x_l)\left(D_n^l(m_l x_l) - D_n^3(m_l x_l)\right)} \tag{3.19}$$

$$c_n^l = \frac{D_n^3(m_l x_l)T_2(m_{l+1}x_l)m_l/m_{l+1} + T_4\left(m_{(l+1)}x_l\right)}{\psi_n(m_l x_l)\left(D_n^l(m_l x_l) - D_n^3(m_l x_l)\right)} \tag{3.20}$$

$$d_n^l = \frac{D_n^3(m_l x_l)T_1(m_{l+1}x_l) + T_3(m_{l+1}x_l)m_l/m_{l+1}}{\psi_n(m_l x_l)\left(D_n^l(m_l x_l) - D_n^3(m_l x_l)\right)} \tag{3.21}$$

Where:

$$T_1(m_{l+1}x_l) = a_n^{l+1}\zeta_n(m_{l+1}x_l) - d_n^{l+1}\psi_n(m_{l+1}x_l) \tag{3.22}$$

$$T_2(m_{l+1}x_l) = b_n^{l+1}\zeta_n(m_{l+1}x_l) - c_n^{l+1}\psi_n(m_{l+1}x_l) \tag{3.23}$$

$$T_3(m_{l+1}x_l) = d_n^{l+1}D_n^l(m_{l+1}x_l)\psi_n(m_{l+1}x_l) - a_n^{l+1}D_n^3(m_{l+1}x_l)\zeta_n\left(m_{l_l+1}x_l\right) \tag{3.24}$$

$$T_4(m_{l+1}x_l) = b_n^{l+1}D_n^l(m_{l+1}x_l)\psi_n(m_{l+1}x_l) - c_n^{l+1}D_n^3(m_{l+1}x_l)\zeta_n\left(m_{l_l+1}x_l\right) \tag{3.25}$$

3.1.3: Asymmetry Parameter

In addition to the differential scattering cross-section $|X|^2/k^2$ used in the definition of (2.15), the asymmetry parameter (g) will also be useful in discussing the scattering behavior. The asymmetry parameter is output by the *scattnlay* program, but its definition is also provided in (3.26). Q_{ext} and Q_{sca} were previously defined by (2.17a,b) and Q_{pr}, dimensionless pressure cross-section, is defined below in (3.17) [18]. For a value of $g = 1$, the system exclusively forward scatters the incident radiation. Conversely, $g = -1$ is exclusive backwards scattering. A value of $g = 0$ signifies equal back and forward scattering.

$$g = \frac{Q_{ext} - Q_{pr}}{Q_{sca}} \tag{3.26}$$

$$Q_{pr} = Q_{ext} - \frac{4}{x_L^2}\sum_{n=1}^{\infty}\left[\frac{n(n+1)}{n+1}Re\{a_n a_{n+1}^{\star} + b_n b_{n+1}^{\star}\} + \frac{2n+1}{n(n+1)}Re\{a_n b_n^{\star}\}\right] \tag{3.27}$$

3.2: Material System

The scope of this work will be limited to the study of metal-dielectric-metal (MDM) noble metal nanoparticles with geometry as shown in Figure 3.1. The refractive index values for the noble metal will be gold (Au) and the dielectric shall be silica (SiO_2) are taken from Johnson and Christy [31] and the Sopra database [32], respectively. Note that for the visible light spectrum, silica is relatively constant, and can be estimated at $(n = 1.46, k = 0)$ if needed. The MDM nanoparticle will be simulated in a host medium of water (H_2O) with $(n = 1.33, k = 0)$ [33].

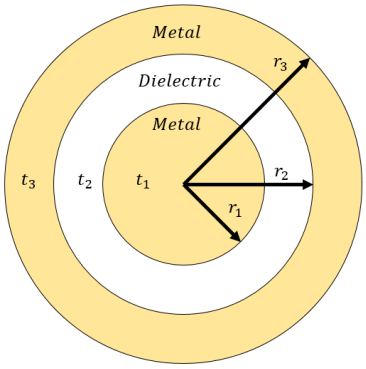

Figure 3.1: Geometric configuration of a metal-dielectric-metal (MDM) nanoparticle, where t_n, r_n represent the thickness and the radii for the n-th = 1…3 layer.

Two main, parametrized configurations will be tested. In both configurations the overall size of the nanoparticle will be fixed at $75\ nm$. In one configuration, the core and dielectric layer will be changed relative to one another, while the outer metal layer is fixed thickness. In the second, the metal core and outer metal layer will change relative to one another, while the dielectric layer

will remain constant. Also, as good practice and as a reference, calculations will be performed for solid gold nanoparticles of similar size. All configurations are displayed below in Table 3.1. Note that the $[35, 15, 25]$ is a duplicate that occurs in both configurations.

Table 3.1: Nanoparticle dimensions

Notes	$t_1\ (nm)$	$t_2\ (nm)$	$t_3\ (nm)$
MDM $Au - SiO_2 - Au$ $t_1 + t_2 = 50$ $t_2 = 10 \dots 35$ $t_3 = 25$	40	10	25
	35	15	25
	30	20	25
	25	25	25
	20	30	25
	15	35	25
MDM $Au - SiO_2 - Au$ $t_1 + t_3 = 60$ $t_3 = 15 \dots 40$ $t_2 = 15$	45	15	15
	40	15	20
	35	15	25
	30	15	30
	25	15	35
	20	15	40
Solid Au Sphere	30	-	-
	40	-	-
	50	-	-
	75	-	-

3.2.1: Complex Refractive Index and Relative Permittivity

The complex refractive index can be expressed in terms of real and imaginary parts n and k, respectively (3.28). The refractive index is linked to the relative permittivity (ε_r) and relative permeability (μ_r) through (3.28), where μ_r is commonly taken as unity for most non-magnetic materials. The relative permeability can also be expressed in real and imaginary parts (3.29) where ε_1 is given by (3.30) and ε_2 is given by (3.31) [34]. Although the refractive index is most commonly associated to optics and the relative permittivity and permeability are associated with Maxwell's equations, the two are ultimately linked. Both the refractive index and relative permittivity will be useful in understanding the response to nanoparticles to light.

$$\hat{n} = (n + ik)^2 = \sqrt{\varepsilon_r \mu_r} \approx \sqrt{\varepsilon_r} \tag{3.28}$$

$$\hat{\varepsilon} = \varepsilon_1 + i\varepsilon_2 \tag{3.29}$$

$$\varepsilon_1 = \frac{n^2 - k^2}{\mu_r} \approx n^2 - k^2 \tag{3.30}$$

$$\varepsilon_2 = \frac{2nk}{\mu_r} \approx 2nk \tag{3.31}$$

Chapter 4: Results and Discussion

Far field and near field calculations were performed for all materials as listed in Table 3.1. As general trends can be seen for each scenario, as well as for the overall MDM material system, only some configurations will be focused on, namely the $[t_1, t_2, t_3] = [35, 15, 25]$, [15, 35, 25], [45, 15, 15] scenarios. The [35, 15, 25] scenario was chosen because it is a moderate scenario that is also shared between both the $t_1 + t_2 = 50$ and $t_1 + t_3 = 60$ cases. The other cases were chosen as fringe cases. The [15, 35, 25] configuration from the $t_1 + t_2 = 50$ case was chosen because it represents the extreme of a thick dielectric layer (and a small core). The [45, 15, 15] configuration from the $t_1 + t_3 = 60$ case was chosen for the converse reason: the metal core is very large. For the cases of the monometallic sphere, the case of $t_1 = 30$ has arbitrarily been chosen as the case of focus if need be and the case of $t_1 = 75$ has been chosen for use as a direct comparison to the multilayered cases.

4.1: Far Field Calculations

Far field calculations were performed for all configurations of focus. Figure 4.1a consists of far field dimensionless efficiencies factors Q_{abs} and Q_{sca} and all curves related to the Fano resonance line fitting procedure (Section 2.3). Figure 4.1b contains the line fit of Q_{sca} to (2.21) and its constituent Lorentzian (2.18) and Fano (2.19) resonances. The parameters obtained from the line fitting procedure can be found in Table 4.1.

The Lorentzian and Fano resonances were found to be centered 2.12 eV ($\lambda = 585.9$ nm) 1.7 eV ($\lambda = 727.8$ nm), respectively. The minimum and maximum of the Fano resonance were found to be at 1.86 eV ($\lambda = 667.1$ nm) and 1.66 eV ($\lambda = 748.9$ nm), respectively. These cases have been plotted against energy in order to give the Fano resonance a better shape.

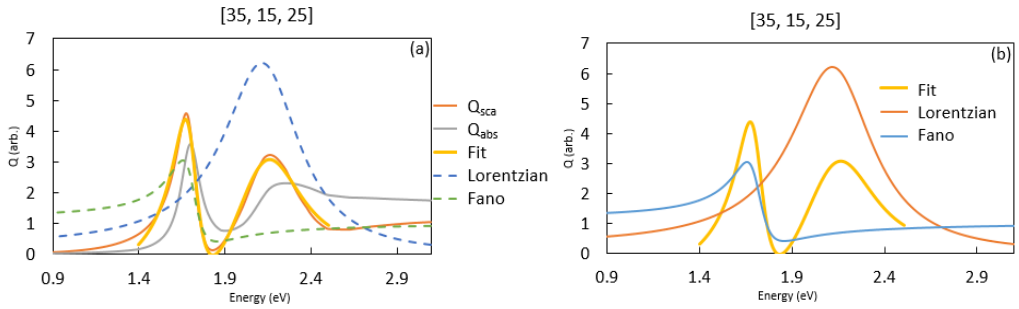

Figure 4.1: (a) Far field dimensionless efficiencies (Q_{abs}, Q_{sca}) and line fit procedure (b) line fit, Lorentzian, and Fano for [35, 15, 25].

Table 4.1: Line fitting parameters of Q_{sca} spectrum of [35, 15, 25].

Parameter	Value	Unit
a	2.50	-
b	1.22	-
q	-1.10	-
E_a	1.70	eV
Γ_a	0.09	eV
E_s	2.12	eV
Γ_s	0.27	eV

Overall, the far field data behaves as expected, in accordance with results from previous studies [16]. For larger particles, such as the $r_3 = 75\,nm$ sized particles studied in this work, scattering is expected to contribute more to the overall Q_{ext} than the absorption (Figure 4.1a). In addition to the magnitude of the peaks, the widths of the peaks should be discussed. The absorption peak is generally sharper than the scattering peak. The broadness of the dipolar antibonding mode (dominated by scattering) interacting with the sharpness of the dipolar bonding one (mainly absorptive) is what causes the Fano resonance, such as that seen in Figure 4.1 [13].

The [35, 15, 25] case is discussed in more detail because it is representative of the general behavior for most MDM cases. The Fano resonance is studied in the scattering spectrum because its appears distorted in Q_{ext} due to the contribution of Q_{abs} [16]. In the scattering spectrum of Figure 4.1a, there exist two predominant peaks. These peaks correspond to the quadrupolar and

dipolar modes for higher and lower energy, respectively, which occur because of the phase retardation effects related to the particle size.

In MDM systems, the interaction between the two metal parts creates a new set of plasmon modes that can be explained using plasmon hybridization theory [16]. Plasmon hybridization theory is a "complementary, mainly qualitative method, where the characteristics of the SPR are explained in terms of interactions between the plasmons of metallic nanostructures of simpler shapes" [16]. The interaction creates the two observed plasmon modes: the dipole-dipole interaction creates the corresponding hybridized dipole mode and so forth for the quadrupolar mode [29].

Note that the bonding peak of the absorption spectrum and the antibonding peak of the scattering spectrum are close to one another (Figure 4.1). Plasmon hybridization in MDM systems causes each plasmon energy mode (e.g. dipolar or quadrupolar) to be associated with a higher-energy antibonding mode and a lower-energy bonding mode. The antibonding mode is wide and dominated by scattering while the bonding mode is narrow and dominated by absorption. In the [35, 15, 25] system, where the relatively wide dielectric layer leads to weak coupling, the bonding mode is determined by the inner nanoshell and the antibonding mode is determined by the outer nanoshell. The two modes overlap spectrally and spatially, which causes Fano resonance to appear.

The Fano resonance region is of importance because very low and very high (in different spectral regions) scattering behaviors can arise. For example, Figure 4.1 shows a Lorentzian peak of large magnitude, which corresponds to what the Q_{sca} would be in absence of the FR. Instead, the observed scattering cross section is greatly diminished in the region around 680 nm, even reaching near-zero values in the central area of the spectrum. Conversely, the scattering around 720 nm is considerably larger than expected.

In the edge cases found in Figure 4.2, the coupling is either too weak ([15, 35, 25]) or too strong ([45, 15, 15]). Both extreme cases made the line fitting procedure fail (Figure 4.2), because neither of the two structures support a Fano resonance. In Figure 4.2a one can visually see how the extreme silica dielectric layer causes a single peak with a small "shoulder". This means that the

silica spacing layer is too thick and the interaction between the LSPR modes of the core and the outer shell is suppressed. The opposite is seen in Figure 4.2b, where there are two separate peaks that do not overlap spectrally. In this case the lack of FR comes from two factors: (i) a thin outer layer means that the mode of the corresponding nanoshell is considerably shifted to the red and (ii) a thin silica layer means that the interaction is strong, shifting apart the bonding and antibonding peaks. Obviously, if both peaks do not overlap spectrally there cannot be an FR.

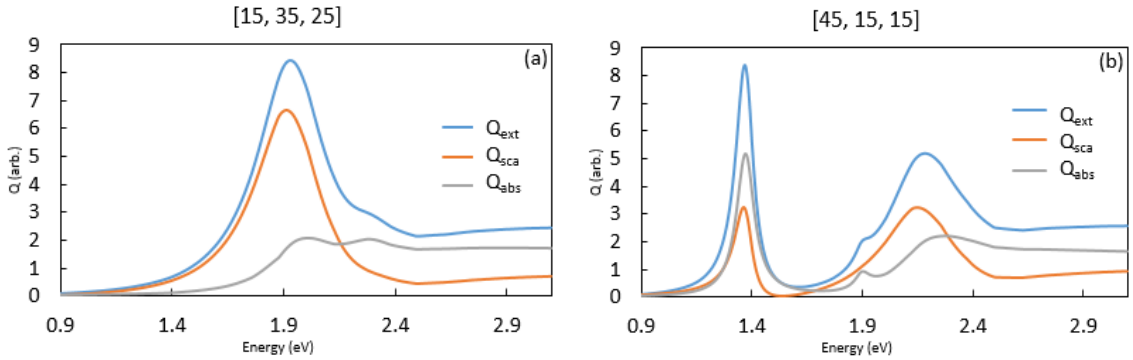

Figure 4.2: Far Field dimensionless efficiencies ($Q_{ext}, Q_{abs}, Q_{sca}$) for t_1, t_2, t_3 = (a) [15, 35, 25] (b) [45, 15, 15]

The behaviors of each system are best visualized by varying parameters leading up to their abnormal behavior (4.3). Figure 4.3a represents $t_1 + t_2 = 50$, with $t_2 = 10 \ldots 35$ and Figure 4.3b represents $t_1 + t_3 = 60$ with $t_3 = 15 \ldots 40$. Note that the figures have been annotated with arrows to highlight the general behavior of each system with their respective changing parameter.

For the first case ($t_1 + t_2 = 50$) we are mainly analyzing the effect of the dielectric layer since the outer layer is kept constant and the LSPR of the core sphere only depends weakly on the size (for this range of radii). Evolution of the FR is illustrated in Figure 4.3a, as t_2 increases from 10 nm until 35 nm. Initially, at $t_2 = 10$ nm there is a clear FR around 820 nm that completely deforms the dipolar LSPR mode and a weak quadrupolar mode that looks like a slight "shoulder". As the dielectric layer becomes thicker, the coupling becomes weaker and the hybridized modes are shifted to the blue (the bonding one) and to the red (the antibonding one), increasing the spectral

overlap between them and shifting the Fano resonance to the blue [16]. However, the reduction of the interaction means that after some point ($t_2 = 20 - 25$ nm) the intensity of the FR reduces, eventually disappearing for the thicker silica layer. Hence, for this case we obtain the nearly-Lorentzian peak seen in Figure 4.1.

The other case studied ($t_1 + t_3 = 60$) keeps the interaction between the modes constant ($t_2 = 15$ nm) but the mode of the outer shell is shifted due to the variations in t_3 [14] the LSPR of the core remains unchanged, as discussed previously. With small t_1, where there is more overlap in the two hybridized energy modes, there is a more intense Fano resonance. As the thickness of the outer shell decreases, the bonding and antibonding modes are shifted away and the interaction between them starts to diminish [16]. Eventually, the two modes do not overlap enough spectrally and have been decoupled, which means that the FR disappears again.

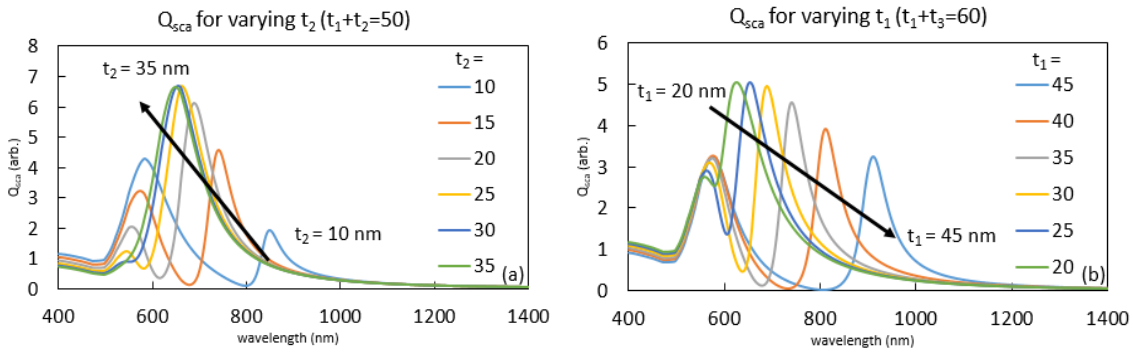

Figure 4.3: Dimensionless scattering efficiencies (Q_{sca}) for (a) $t_1 + t_2 = 50$ and (b) $t_1 + t_3 = 60$.

The line fitting parameters, as discussed in Section 2.3, were plotted against varying geometric parameters in Figures 4.4-4.6 as supplements for discussion. Note that for 4.4a-4.6a, the line fitting procedure failed for $t_2 = 30, 35$ and for 4.4b-4.6b, the quality of the line fit for $t_1 = 45$ was poor and thus not used. Note that the lines connecting discrete points are merely a guide to the eye and parameters were calculated only for configurations as discussed in Table 4.1. The quantitative values of the line fitting parameters can be found in Appendix A.

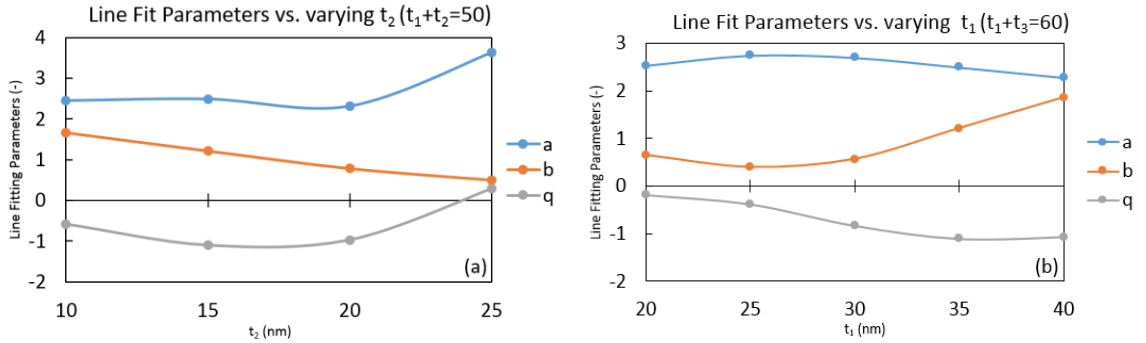

Figure 4.4: Line fitting parameters for (a) $t_1 + t_2 = 50$ and (b) $t_1 + t_3 = 60$

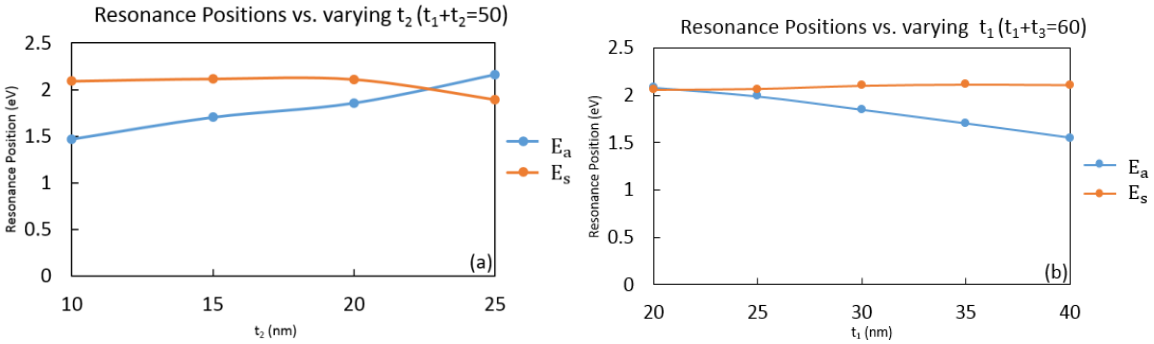

Figure 4.5: Resonance positions for (a) $t_1 + t_2 = 50$ and (b) $t_1 + t_3 = 60$

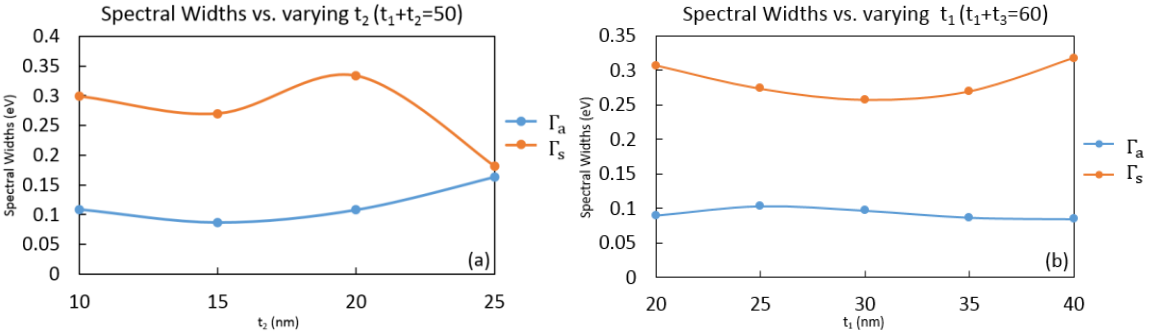

Figure 4.6: Spectral widths for (a) $t_1 + t_2 = 50$ and (b) $t_1 + t_3 = 60$

The increasing effects of the increasing dielectric layer can be seen in Figures 4.4a-4.6a. As has been discussed, a thick dielectric layer weakens interaction between the core and the shell, thus weakening the Fano resonance. As a result, the scattering mode of the outer shell, which is closely Lorentzian, dominates. The eventual dominance of the scattering Lorentzian peak is evident

by observing a and b of Figure 4.4, where the Lorentzian peak grows greatly in magnitude after a threshold $(t_2 = 20 - 25)$ and the Fano resonance begins weakens (b) until its eventual disappearance. Furthermore, the blue-shifting of the Fano resonance caused by the increasing spectral overlap of the bonding and antibonding peaks can be confirmed by observing its position E_a in Figure 4.5a. In contrast, the Lorentzian peak position stays relatively constant.

The effect of the changing outer layer on the spectral overlap of the energy modes is illustrated in Figures 4.4b-4.6b. As the outer shell becomes thinner, the Fano resonance appears to red-shift away from the Lorentzian peak. The FR, which is actually as a result of the interaction between the bonding/antibonding modes, are shifting away from one another, eventually causing the FR to disappear because there is not sufficient spectral overlap. As expected, in all cases the spectral width (Figure 4.6) of the Fano resonance was smaller than the Lorentzian peak.

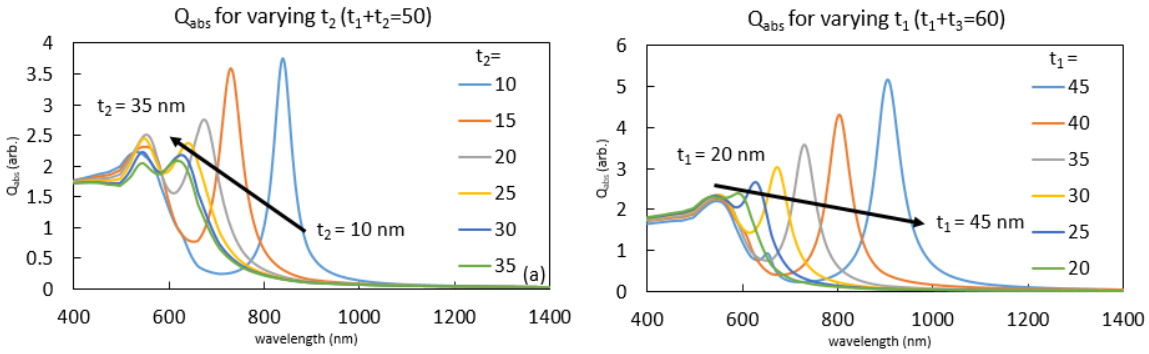

Figure 4.7: Dimensionless absorption efficiencies (Q_{abs}) for (a) $t_1 + t_2 = 50$ and (b) $t_1 + t_3 = 60$.

The effects of changing geometry on the absorbance spectrum have been plotted in Figure 4.7. Note that the absorbance spectrum is not affected by the Fano resonance. Hence, the evolution of the dipolar bonding mode can be seen clearly here. It can be verified that the maximum of the absorption corresponds approximately to the center of the FR, when the latter appears.

The increasing dielectric layer of Figure 4.7a shows the damping of the LSPR as it overlaps spectrally with the interband transitions. At a small thickness, the strong interactions red-shift the bonding mode, far from the region of interband transitions of gold, and there is a strong, sharp peak.

However, within a small change at $t_2 = 20$, the LSPR blue-shifts and overlaps with the interband transitions; hence, the magnitude and presence of the peak has almost disappeared. Figure 4.7b shows behavior to a similar effect, but while the dielectric layer is held constant. In this case, the outer shell is responsible for the observed shifts, which is red- (blue-) shifted as its thickness decreases (increases). In both cases, the absorbance exhibits a singular, strong peak, as opposed to the Lorentzian peak modulated by the FR in the scattering spectrum.

Far field calculations were also performed for all cases of the monometallic gold sphere, but without Fano resonance fitting procedure, as it is not expected to occur (Figure 4.8). Compared to the dimensionless absorption efficiencies of MDM systems, monometallic gold is significantly blue shifted.

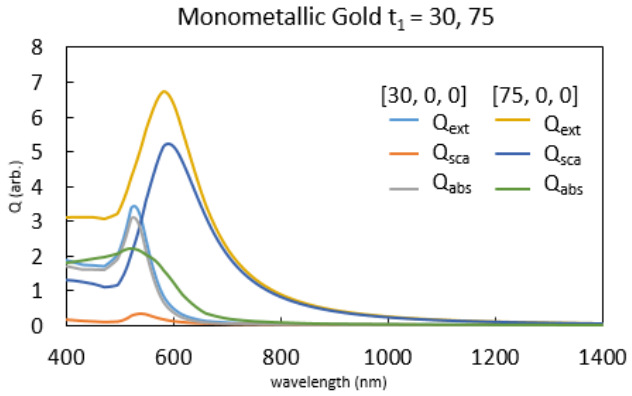

Figure 4.8: Far field dimensionless efficiencies ($Q_{ext}, Q_{abs}, Q_{sca}$) for solid gold (Au) sphere for $t_1 = 30, 75$.

The cases of monometallic spheres help explain the relationship between absorption and size. One can see the high contribution of Q_{abs} to the Q_{ext} for $t_1 = 30$ (Figure 4.8), where the two are nearly identical. On the other hand, when t_1 has reached 75 nm in Figure 4.8, the scattering contribution dominates, while the absorption peak has been also dulled. The same configuration ($t_1 = 75$ nm) can be directly compared to the MDM cases. In contrast to the MDM spectra, there is no existence of two energy modes (hybridization) and significant blue shifting of the maxima.

4.1.1: Reduced Differential Scattering Cross-Section & Asymmetry Parameter

The reduced differential scattering cross-section, shown in polar coordinates, can be seen in Figure 4.9 for the case of [35, 15, 25]. The angle 0° represents forward scattering, while 180° represents backward scattering. Although understanding of the overall spectral behavior of a nanoparticle is best given by g, the asymmetry parameter (3.26). As can be seen in Figure 4.10 for the same structure, the asymmetry parameter also exhibits a Fano resonance, which is slightly blue shifted with respect to the one observed in the scattering spectrum (also shown in the plot, arbitrarily scaled down).

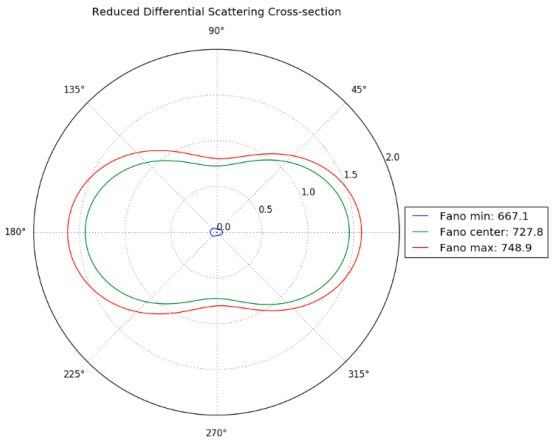

Figure 4.9: Reduced differential scattering cross-sections for (a) [35, 15, 25] at three wavelengths. The angle 0° represents forward scattering, while 180° represents backward scattering.

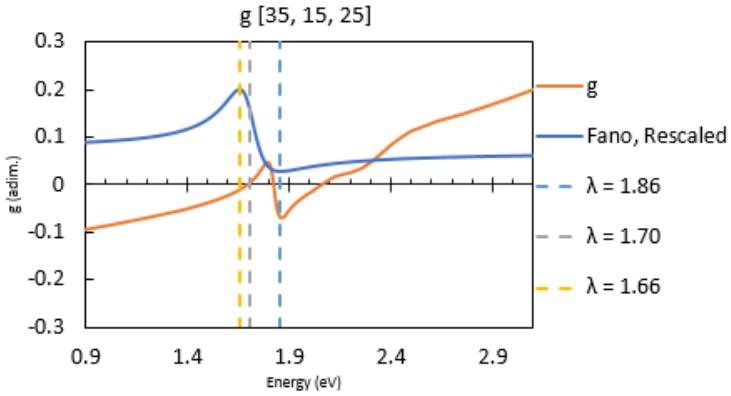

Figure 4.10: Asymmetry parameter and arbitrarily rescaled Fano resonance for [35, 15, 25], with min, center, and max and center Fano resonance lines.

The reduced differential scattering cross-section of Figure 4.9 was calculated at the three Fano points. Noticeably, the minimum of the Fano resonance has extremely small scattering, while the center and the maximum have similar magnitudes to each other. The behavior is readily explained by looking at the far field spectrum for the same material in Figure 4.1. The minimum of the Fano resonance is very close to the minimum of the scattering, which is nearly zero. Simply put, the magnitude of scattering is already low. Meanwhile, the Fano center and Fano maximum are close together in the spectrum, differing only by about 20 nm. The Fano center and maximum are in proximity to the maximum scattering, with the maximum of the Fano resonance being the closest. Correspondingly, the maximum Fano resonance has the greatest reduced differential scattering cross-section.

In the larger spectrum (Figure 4.10), the asymmetry parameter delivers a more comprehensive understanding. Interestingly, the minimum of the Fano resonance ($\lambda = 667.1$ nm, $E = 1.86\ eV$) coincides with the local minimum of g. Here, there is the most backscattering ($g \approx -0.1$) but the total scattering is already very low, which means that the detrimental backscattering is negligible. In this area, the absorption is also relatively low (Figure 4.1). Physically speaking, more light is reflected in the Fano resonance minimum than at other wavelengths in the vicinity. The center of the Fano resonance seems to relate to the point of even backscattering and forward scattering ($g = 0$), but the maximum of the Fano resonance has no obvious implications.

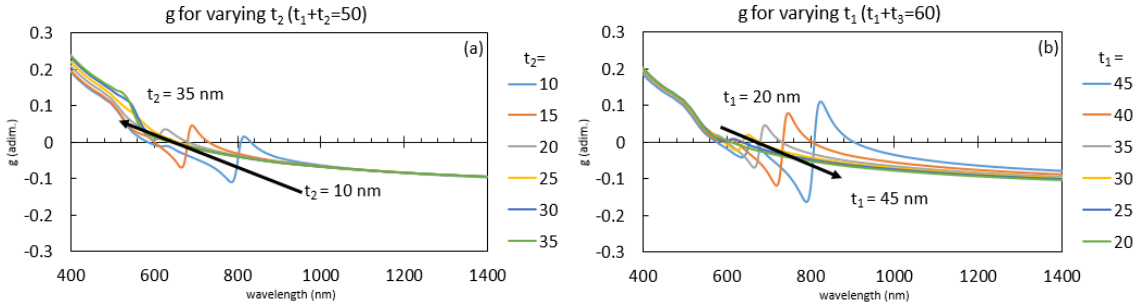

Figure 4.11: Asymmetry parameter spectra for (a) $t_1 + t_2 = 50$ and (b) $t_1 + t_3 = 60$.

The behavior of the geometry on the asymmetry parameter was also studied. The asymmetry parameter, as calculated by *scattnlay* according to (3.26), for all the MDM configurations is shown in Figure 4.11 for (a) $t_1 + t_2 = 50$ and (b) $t_1 + t_3 = 60$. For both figures, at lower wavelengths (below 600 nm) forward scattering is dominant, and the converse is true at higher wavelengths. Simply put, the higher energy light at lower wavelengths will be more likely to penetrate forward into the material when compared to a weak light that will be preferentially backscattered. In both cases, the FR in the asymmetry parameter follows exactly the same trends as the one observed in the scattering efficiency and the discussion will not be repeated here. The only noticeable difference is that this FR is considerably sharper, producing a quick change in the sign of g over a short range. Note that asymmetry parameter plots for monometallic spheres (Figure 4.12) do not show this behavior. Instead, the asymmetry parameter monotonically decreases over the spectrum.

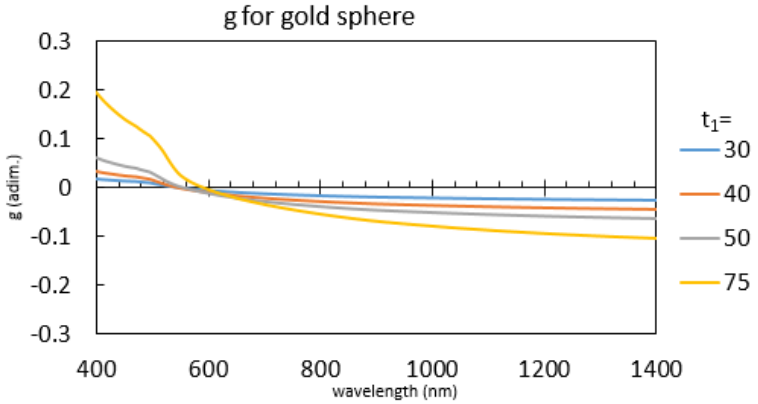

Figure 4.12: Asymmetry parameter spectra for solid gold (Au) sphere for $t_1 = 30, 40, 50, 75$ nm.

The scattering benefits of the tuned MDM nanoparticles over their monometallic counterpart can be quantified by finding the difference in their symmetry parameter. For all configurations the change in g of the MDM nanoparticles from monometallic gold of the same size were calculated. In Figure 4.14 the comparison of the $[35, 15, 25]$ configuration to monometallic

gold is made. Figure 4.15 displays the effect of the changing geometry on g. Values closer to zero represent closer behavior to the monometallic case.

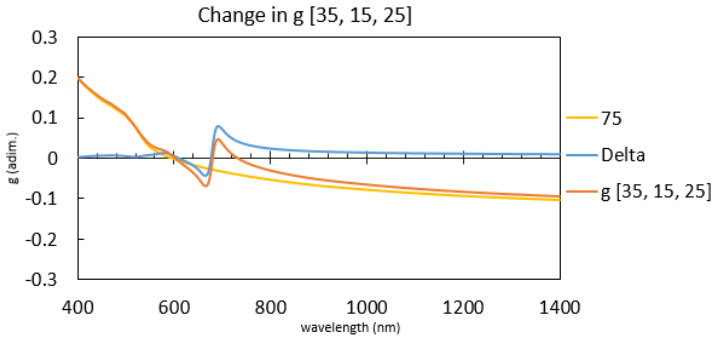

Figure 4.13: Comparison of symmetry parameters between [35, 15, 25] MDM and $t_1 = 75$ nm gold sphere

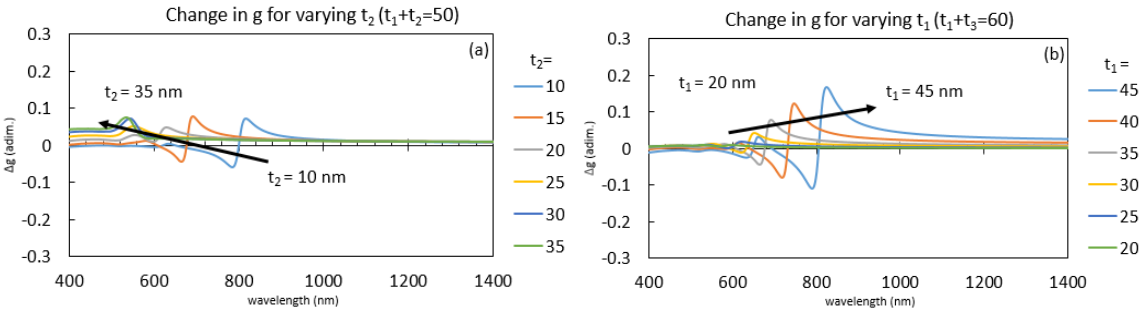

Figure 4.14: Change in g of MDM nanoparticles from $t_1 = 75$ nm gold sphere of the same size

In Figure 4.13, an improvement in g can be seen across the spectrum, except for in the vicinity of the Fano minimum. The improvements are especially seen in the infrared region, where the Fano maximum is located. Conveniently, the infrared spectrum of sunlight (Figure 2.1) is typically difficult to capture, while the high energy region already features strong forward scattering behavior. Again, the detrimental effects seen near the Fano minimum are diminished due to reduced scattering.

Similar behavior to Figure 4.13 was seen for all configurations in Figure 4.14. For the case in (b) $t_1 + t_3 = 60$, the magnitudes of the peaks were greater than that of (a). Figure 4.14a showed weakly beneficial behavior at higher energies when compared to the monometallic case.

4.2: Near Field Calculations

As was the case for the reduced differential scanning cross-section, the near field color maps showed relatively similar behavior to one another. Only the [35, 15, 25] case has been shown below, calculated at the minimum ($\lambda = 667.1$ nm) (Figure 4.15), center ($\lambda = 727.8$) (Figure 4.16) and maximum ($\lambda = 748.9$ nm) (Figure 4.17) of the Fano resonance (Figure 4.1). At each wavelength, both the field enhancement (figures (a) on the left) and the Poynting vector (figures (b) on the right) were calculated. The magnification of electric field can be calculated by dividing the electric field around and inside the particle by the incident electric field, i.e. $|E|/|E_0|$. The particles were irradiated by an x-polarized wave. Visually, the wave propagates from left to right ($-Z$ to $+Z$). Although a 3D problem, only the X-Z plane ($Y = 0$) has been shown, as behavior is not expected to move or differ out of plane, according to the symmetry of the problem [35].

The color maps representing the Poynting vector (power flux) are calculated according to (2.6). The color gradient represents the magnitude of the Poynting vector. In some figures, take note of the termination of the power flow lines inside the sphere, representing a loss of power. An arbitrary number of power flow lines were used, so the behaviors of the lines are not representative of the complete behavior. At high and low values of wavelengths, the power flow lines passing by the particle represent more light passing by with limited interaction with the particle. Additionally, notice that some lines enter trajectories forming "vortices" that spiral inwards until termination.

Additionally, a wider spectrum of the field enhancement has been calculated for points just outside the surface ($\approx 0.05\ nm$ away) of the metallic inner core and metal outer shell (Figure 4.18). The surface of each metallic layer is where the maximum values are expected to occur (along the line $Z = 0$). The maximum values of each spectrum were also found. A maximum enhancement of 39.6 was found at $\lambda = 726$ nm for the inner core and a maximum enhancement of 8.1 at $\lambda = 747$ nm was found for the outer layer.

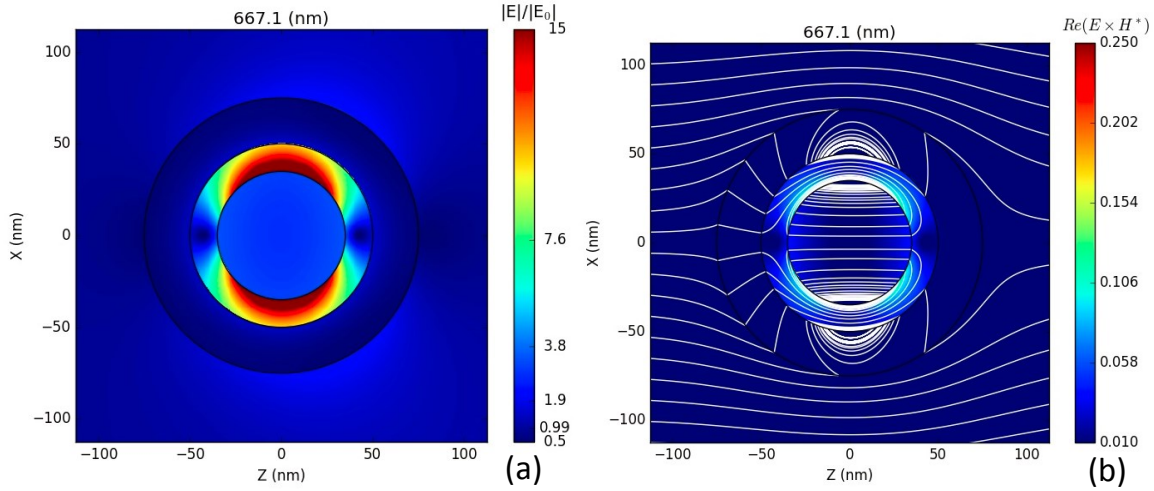

Figure 4.15: Near field color maps of (a) field enhancement and (b) power flow for the minimum ($\lambda = 667.1$ nm) of the Fano resonance of [35, 15, 25]

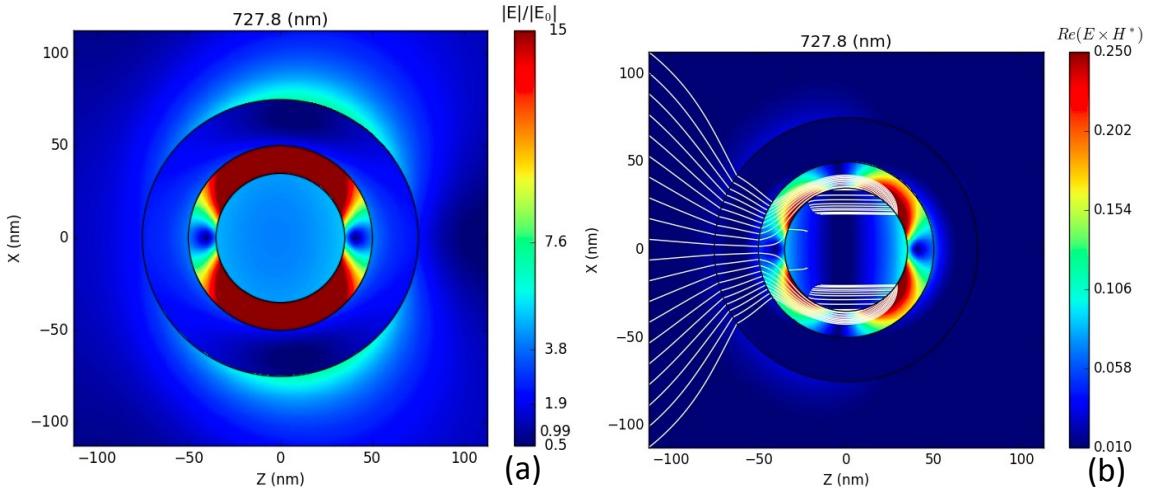

Figure 4.16: Near field color maps of (a) field enhancement and (b) power flow for the center of the Fano resonance ($\lambda = 727.8$ nm) of [35, 15, 25]

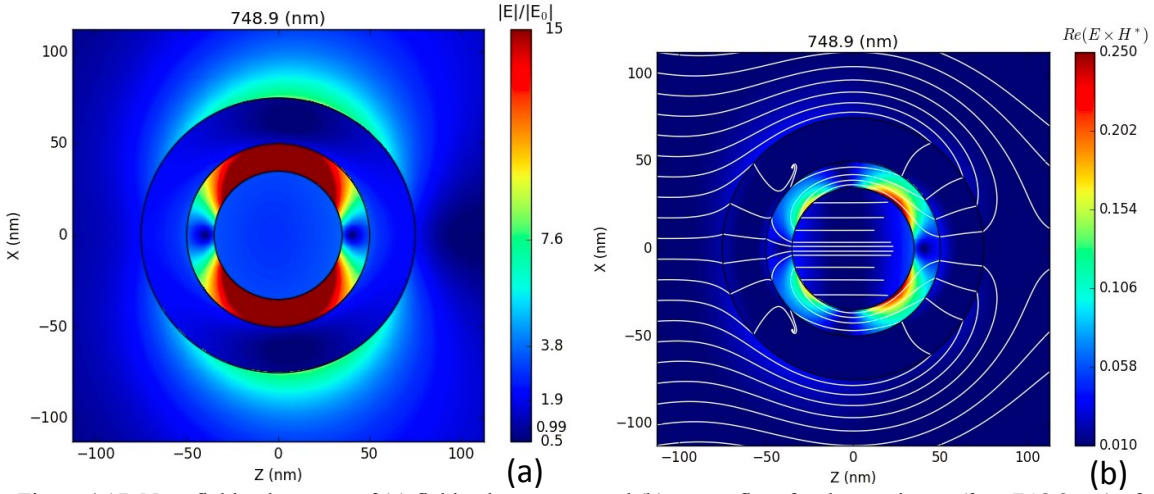

Figure 4.17: Near field color maps of (a) field enhancement and (b) power flow for the maximum ($\lambda = 748.9$ nm) of the Fano resonance of [35, 15, 25]

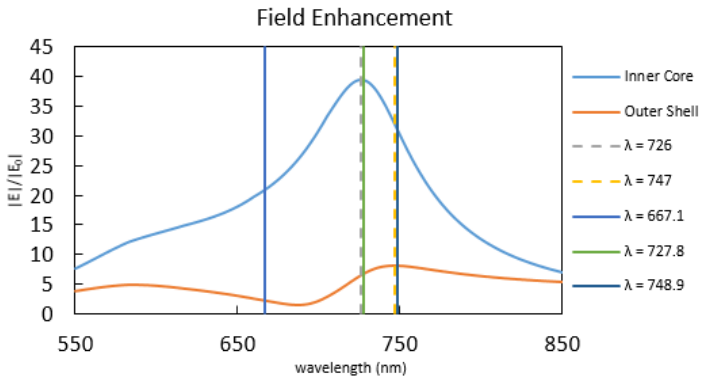

Figure 4.18: Field enhancement on surface of metallic layers vs. wavelength for [35, 15, 25] MDM nanoparticle. The dashed vertical lines maximum values on the surface of the metal layers. The solid vertical lines represent the three Fano points.

The near field benefits of plasmonic nanoparticles lie within their field enhancement. Effectively, they act as antennas by absorbing light and reradiating it in their vicinity at greater intensity. Figures 4.15a-4.17a depict the electromagnetic field in the near field region at three wavelengths throughout the Fano spectrum, while Figure 4.18 shows the maximum field enhancement over an entire spectrum. In every figure, most of the field enhancement activity occurs in the dielectric layer, specifically at the surface of the core.

Plasmonic behavior is also seen on the surface of metal shell, albeit not as strongly. By looking at the flow of power shown in 4.15b-4.17b, especially at the minimum and maximum of

the Fano resonance, the metal shell acts as a lens on which light is focused onto the metallic core. In fact, in some cases, the power flow travels *backwards*, interacting several times with the nanoparticles. Additionally, the outer shell is hindered by the weaker host medium (water, $n = 1.33$) compared to silica ($n = 1.46$).

In the larger view shown in Figure 4.18, the field enhancement of the core is less sporadic than the far field behavior, especially when referencing the peak behavior demonstrated by the core. The figure confirms that the minimum of the Fano resonance represents a smaller enhancement than at the center or maximum of the Fano resonance. The center of the Fano resonance is shown to be strongly related to, but not exactly, the maximum enhancement. On the other hand, the maximum of the Fano resonance looks to be correlated to the maximum of the field enhancement in the outer shell. Hence, it is clear that there is a direct relation between the scattering and the field enhancement, as some other authors have pointed out [36, 37]. The small discrepancies seen between the far field (center and maximum of the Fano resonance) with the maximum near field enhancements (of the metal core and shell) have been previously reported in other systems [7]. Unfortunately, the behavior has not been fully explained. The center of the Fano resonance can be reasonably approximated as the location of the maximum absorption, as discussed in Section 2.3. The maximum of the absorption, at $\lambda = 728.9$ nm was found to be very close to the actual value of $\lambda = 727.8$ nm.

The power flow of 4.15b-4.17b allows a closer view of the behavior seen behind the field enhancement. In Figure 4.16b, almost all power lines move into the sphere and core, whereas for lower field enhancements of Figure 4.15b and Figure 4.17b, more power lines are seen passing the nanoparticle with limited interaction, and more interaction is seen with the shell. In Figure 4.17b, notice the presence of dead-end power lines. This contrasts to the Fano center, where the maximum field enhancement can be interpreted as using more light for generating LSPR.

One of the peculiar features in the power flow plots of Figures 4.15b-4.17b is the existence of the vortices. The vortices are physically interpreted as light circling around, interacting with

particles multiple times. The effect manifests in the dimensionless efficiencies, where the particles seem “larger” than they actually are. The existence of these “nanoscale optical vortices” in the vicinity of the plasmon resonance have been reported before in pure metallic nanoparticles [35]. These vortices have been reported to take two forms: inward vortices and outward vortices. Outward vortices enter the particle near the center line, turning away from the center line upon exiting, and finally spiral inwards until termination. Inward vortices first pass the particle, turning towards the center line, and entering around the back of the particle before spiraling. Outward vortices were reported for wavelengths below the LSPR, while inward vortices were reported for wavelengths above the LSPR [35]. However, note that for the LSPR of the gold core, only inward vortices were observed. In Figure 4.15b-4.17b, the powerlines travel around and pass the sphere before entering towards the back and spiraling inwards. Resemblance of an outward vortex are seen in Figure 4.15b, but pale in comparison to the observed inward vortices in the same figure. The vortex direction has been found to depend on the real and imaginary parts of the metal’s complex dielectric function [35].

Figure 4.19 contains the refractive indices and the corresponding calculation of permittivity for gold. The real and complex parts of the refractive index have been plotted in Figure 4.19a, as obtained from Johnson and Christy [31]. Accordingly, the real and complex parts of the relative permittivity have been calculated according to (3.28)-(3.31) and plotted in Figure 4.19b. The minima of the real refractive index (n) and imaginary permittivity (ε_2) have been found at 705 nm and at 660 nm, respectively. Because of the resolution of the data set, these two values are actually adjacent to one another.

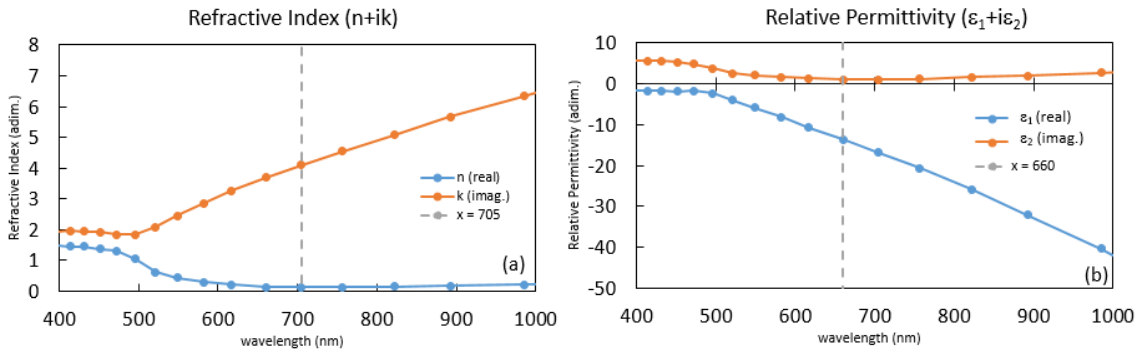

Figure 4.19: Real and imaginary parts of the complex (a) refractive index values and (b) relative permittivity

The refractive indices of gold reported by Johnson and Christy were compared to experimental values [31]. They note that true LSPR occurs under the conditions of $\varepsilon_1 = 0$ and $\varepsilon_2 \ll 1$ if one uses the relative permittivity or $n = k$ and $k < 1$ if one is using the refractive index, which occurs in silver, but not in gold. They emphasize that the LSPR differs from the plasma frequency predicted by the free-electron, or Drude model [31]. Indeed, there is no point where the real refractive index crosses the imaginary part (the $n = k$ condition) in Figure 4.19a, nor is k ever less than 1. Instead, the vortices are observed in the vicinity of the minimum of the real refractive index ($n,\ \lambda = 705$ nm) and minimum of the imaginary dielectric constant ($\varepsilon_2, \lambda = 660$ nm). Again, these values are adjacent.

The observation of only inward vertices over a spectrum implies peculiar behavior with respect to the LSPR frequency. The discussion of the existence of LSPR in nanoparticles suboptimal conditions has been explained using spectral representation formalism in the quasistatic limit ($r < 50$ nm) [33]. The quasistatic assumption applies to nanoparticles that have a diameter much smaller than the wavelength of the incident electromagnetic field, causing them to feel a field "spatially constant but with a time-dependent phase" [33]. The goal of their approach was to parameterize the study of nanoshells by separating the responses relating to geometry from those of the dielectric properties. As a result, spectral representation formalism is able to produce information about both the frequencies and the weight of the coupling of the external field to the SPR [33]. The polarizability of the nanoparticles is described using a spectral parameter, $s(\omega)$. The

spectral parameter is defined in (4.1), where ω is the frequency, $\varepsilon(\omega)$ is the frequency dependent complex dielectric constant, and ε_h is the dielectric constant of the host medium.

$$s(\omega) = \frac{1}{1 - \frac{\varepsilon(\omega)}{\varepsilon_h}} \tag{4.1}$$

In their framework, they observe that for the scenario of gold in water, optimal conditions for LSPR are not reached: the real part of the spectral parameter does not reach an eigenvalue requirement at the same time the imaginary part of the spectral parameter is much less than 1. Instead, LSPR is observed at a condition where the real part is as close as possible to the eigenvalue requirement while the imaginary part is minimal. Agreeing with Johnson and Christy [31], the authors show that the LSPR condition for silver is fully met. The LSPR manifests itself on the far-field spectrum as peaks in the absorbance cross-section, with silver having much stronger peak behavior than gold.

The study of the LSPR of gold is extended by calculating the behavior in different dielectric mediums. As the dielectric medium's refractive index increases in magnitude (at values greater than $n = 1.46$ observed in silica), the LSPR condition involving the eigenvalue is easier reached. However, the strongest LSPR occurs when the second condition is also fulfilled, in that the imaginary part of the spectral parameter occurs when the material is the least lossy ($\varepsilon_2 \ll 1$). In the MDM system studied in our work, analogous behavior can be interpreted. In Figure 4.22b, ε_1 decreases continuously, so the LSPR condition is best met when the imaginary part ε_2 is minimal. When ε_2 is minimal, the least light is loss at this point.

Much of the behaviors observed in MDMs can be verified by comparing them to particles of similar size. The near field calculations were performed for monometallic gold spheres of $t_1 =$ 30 and 75 nm at $\lambda = 526.2$ nm (Figure 4.20) and $\lambda = 625.0$ nm (Figure 4.21), respectively.

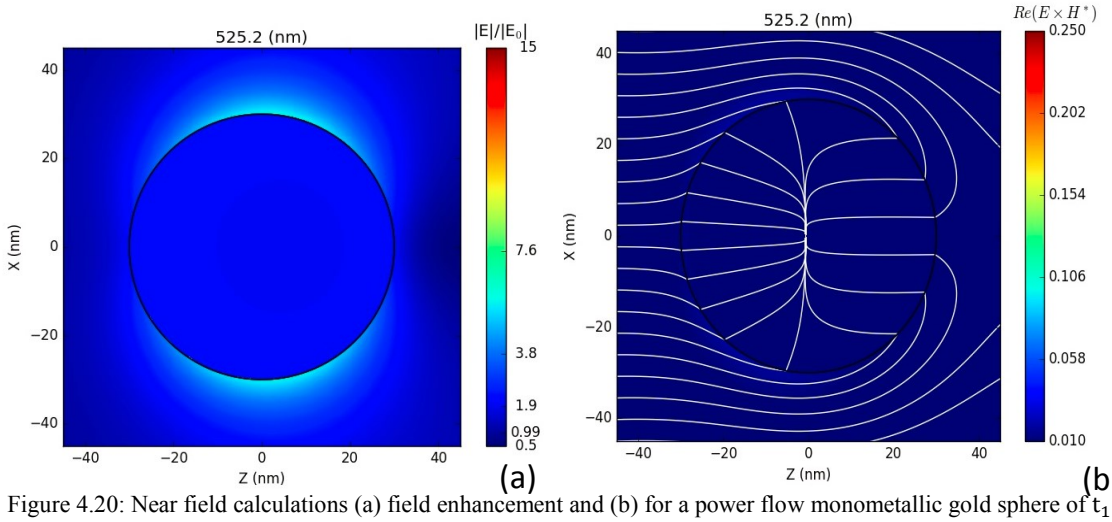

Figure 4.20: Near field calculations (a) field enhancement and (b) for a power flow monometallic gold sphere of $t_1 = 30$ nm at maximum absorption ($\lambda = 526.2$ nm)

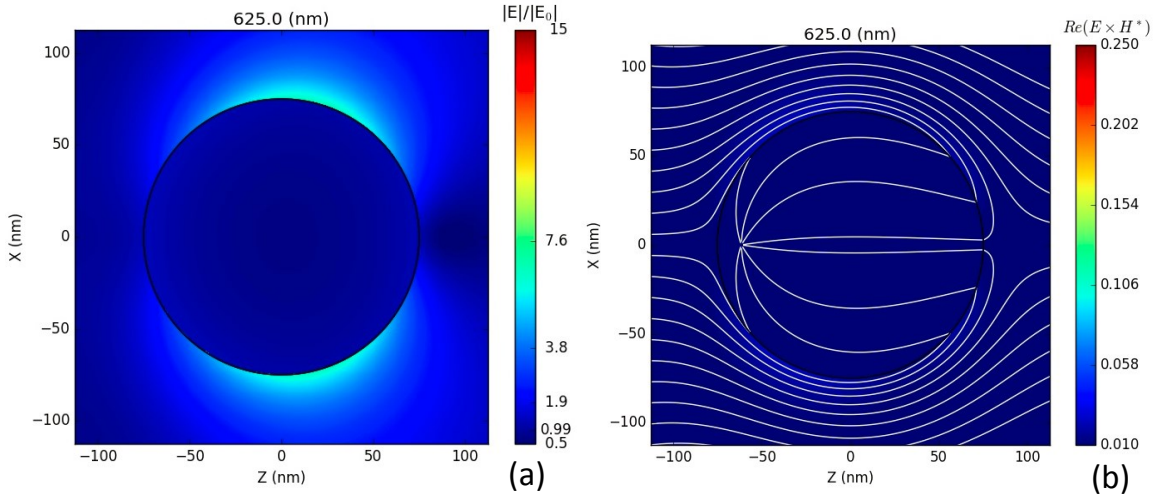

Figure 4.21: Near field calculations (a) field enhancement and (b) for a power flow monometallic gold sphere of $t_1 = 75$ nm calculated near the maximum enhancement ($\lambda = 625.0$ nm).

The monometallic cases of Figure 4.20 and Figure 4.21 show field enhancements, like the MDM, but much weaker. The enhancement of the monometallic cases is approximately 5-6x, as opposed to 8.1x and 39.6x for the shell and core of Figure 4.16, respectively. The difference in strength is due to the weaker dielectric medium (water) and due to the lack of the outer shell for which the core can couple with. Compared to Figures 4.15-4.17, there is no outer shell to "focus"

the light onto the core. The monometallic sphere in water is of similar magnitude as the shell, but nonetheless does not reach levels of the MDM core.

Additional calculations were performed for the $t_1 = 30$ nm at an arbitrary wavelength ($\lambda = 555$ nm) to emphasize the vortex behavior seen in plasmonic nanoparticles (Figure 4.22).

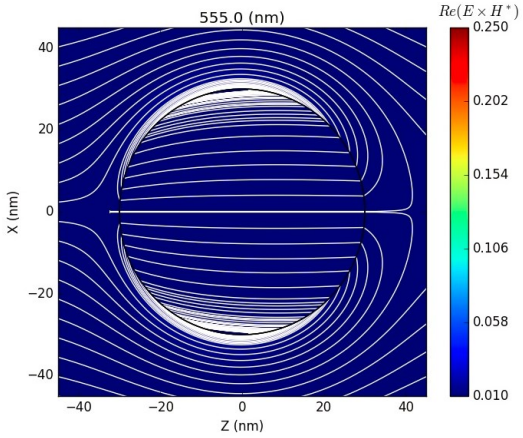

Figure 4.22: Inward vortices in power flow near field calculation of a monometallic gold sphere $t_1 = 30$ nm at an arbitrary wavelength

For this case, near field calculations were performed for a wide spectrum and no evidence of outward vortices were found, confirming the conclusions reached from the discussion of suboptimal LSPR conditions [33, 35].

4.3: Far Field vs. Near Field in Solar Cells

Both far field and near field behavior for MDM nanoparticles were studied as prospects for use in plasmonic solar cells (PSCs). The two proposed configurations to make best use of their properties are either on the surface layer to scatter and trap light (Figure 1.3a) or as antennas to locally magnify incident light (Figure 1.3b). The largest difference between the two phenomena for an MDM system is how each behavior occurs.

Idealistic scattering behavior would be: 100% forward scattering ($g = 1$) past the critical angle of 16° for a silicon-air interface and a maximized scattering cross section Q_{sca} across the

spectrum of visible light. On the other hand, idealistic near field behavior would be: maximum field enhancement in a spectrum that matches visible light. The results obtained for MDM nanoparticles were not optimal, but still considerably better than those obtained for the solid gold sphere. This means that MDM structures will provide an enhanced efficiency for plasmonic solid cells in any of the two possible configurations. More importantly, the optical response of those structures can be tuned by means of the geometrical parameters. In this way, even if the region with the larger improvements is relatively narrow, it will not be hard to design an ensemble of nanoparticles able to improve the efficiency for the full solar spectrum (Figure 2.1).

In the visible light spectrum, the scattering of the light was mostly forward (up to $g = 0.2$) especially at lower wavelengths (Figure 4.10). In the Fano resonance area, the behavior showed brief spectral regions of both preferential forward and backward scattering. However, the detrimental effect of backward scattering, which occurs around the FR minimum, is mitigated because the scattering is also locally minimized here. The preferentially forward scattering region replaces the preferentially backwards scattering behavior seen in a solid gold sphere of the same size (Figure 4.12). An improvement of up to $\Delta g = 0.787$ was observed when comparing the asymmetry spectra in this region. The benefits of the forward scattering are increased even further when nanoparticles are placed as shown in Figure 1.3a, as light would scatter favorably forward into the dielectric of higher permittivity [9]. For the reduced differential scattering cross-section, the magnitude in the direction of exact forward (0°) and backward (180°) scattering is largest and smallest perpendicular to that. The shape of the reduced differential scattering cross-section shows that much of the light travelling forward is still scattered at the critical angle (16°). The light scattered passed this angle will remain inside the solar cell.

For the same spectrum, there was consistent electric field enhancement through LSPR. Although the most intense enhancement in MDM systems occurs in the dielectric layer, the outer metal shell shows an enhancement of roughly 8x (Figures 4.16, 4.19) versus enhancements of 5-6x observed solid metal nanoparticles (Figures 4.20, 4.21). These benefits are best exploited in the

configuration shown in Figure 1.3b. It is worth mentioning that the absorption process for generating LSPR will also lose energy through the generation of heat, as opposed to the reradiation in scattering.

Chapter 5: Conclusions

Harnessing the huge energy of the sun through photovoltaics is an increasingly important subject. The current dominant technology in this field is crystalline silicon, while thin-film solar cells are limited by their ability to absorb near-band gap light. This flaw could be remedied through the use of noble metal nanoparticles supporting tunable Fano resonances in order to trap light and increase the absorbance efficiency. Noble metal nanoparticles have two key behaviors to exploit: their far field scattering and near field enhancement. Such solar cells are named, "plasmonic solar cells" (PSCs). These two behaviors are strongest in the vicinity of the Fano resonance area. The Fano resonance in symmetric MDM structures occurs due to the interaction of the wide antibonding energy mode and the narrow bonding energy mode. Inside this regime,nanoparticles can show peculiar behavior, such as the extremely low or high scattering. The Fano resonance spectrum can be tuned in those structures to better match the requirements of a PSC. For instance, the resonance can be tuned to assist the absorbance of near bandgap light in the semiconductors, or so that the far field behavior matches the sun's light spectrum. The behavior of light interacting with small particles can be predicted exactly by analytical expressions derived from Mie theory calculations. Hence, it is possible to use computational simulations to design and optimize structures for enhancing the efficiency, which saves time and resources.

In this work, we studied the Fano resonances that appear on MDM gold-silica-gold nanoparticles in water using *scattnlay*, a computational Mie theory program. A variety of configurations of MDM nanoparticles were analyzed. The far field extinction, scattering, and absorption cross-sections were calculated. The scattering spectrum was fit with an equation representing the convolution of its Lorentzian and Fano peaks, allowing the Fano resonance to be isolated. In the far field, the scattering behavior was focused on by calculating the reduced differential scattering cross-section and asymmetry parameter. The near electric field enhancement was studied to understand the promise of plasmonic nanoparticles and the near field Poynting vector was calculated in order to understand the mechanisms behind the field enhancement.

In the far field, quadrupolar and dipolar modes exist as a result of the phase retardation effects from the particle size. The interaction between the metals components in MDM nanoparticles create new energy modes. The two energy modes are explained using plasmon hybridization theory, but only the dipole mode was studied, as it related to the LSPR. The dipole mode contained narrow bonding and wide antibonding orbitals which were dominated by the absorption and scattering spectra, respectively. When these modes overlapped, Fano resonance appeared.

The thickness of the dielectric layer determined the coupling strength of the core and shell, and thus, affected the Fano resonance. At smaller thicknesses, the interaction can be much stronger, but the energy modes can be shifted away from one another without spectral overlap, causing the FR to disappear. As the dielectric thickness increases, the modes move closer to one another. At large thicknesses, the interaction becomes weak, and again, the FR disappears. In the absorption spectrum, increasing thickness showed the damping of LSPR as it blue shifted towards the interband transition region.

When the thickness of the dielectric layer was held constant, the effect of the relative size of the outer metal layer could be examined. At a smaller outer layer, there is overlap between the two hybridized energy modes and a more intense Fano resonance. With increasing thickness, the modes are shift away from one another, eventually not having sufficient spectral overlap for FR.

The center and width of the unperturbed LSPR (the Lorentzian peak) and the FR were extracted by fitting the scattering spectra. The other points of interest on the Fano curve were the minimum and maximum. Calculation of the reduced differential scattering cross-section revealed an FR that considerably increases the forward scattering in a high-scattering region whereas the increase of backscattering occurs for a region with virtually no scattering. This means that MDM improve considerably the situation with respect to the solid nanoparticles. A sizeable portion of light scatters past the critical angle for a silicon-air interface, but no preference was seen.

In the near field, the center of the Fano resonance, was found to correspond to the maximum field enhancement in the intermediate shell. The maximum of the Fano resonance (i.e., the maximum scattering) corresponded with the maximum of the surface plasmon resonance on the outer shell. The correspondence was close, but not exact, as there exists a discrepancy between the nearfield and far field behavior. The larger field enhancement was found to occur on the surface of the inner core; however, MDM nanoparticles showed important improvements over their monometallic counterparts. In this system, power flow lines indicated the purpose of the outer metallic shell that focused light on the core. Regardless, the outer shell still saw an 8-fold field enhancement at its best. The power flow lines also highlighted the existence of vortices, which only manifested themselves as the inward variety [35]. The power flow lines indicate that, close to the LSPR frequency, the light passes through the particle multiple times, effectively raising the absorption cross-section. The inward-only behavior occurs because the optimal conditions for LSPR do not exist for gold in silica or water. Instead, the observed LSPR occurs when the conditions are met closely enough, namely around the area where the real part of the refractive index is minimal.

Both solar cell design configurations analyzed in this work improve the efficiency, by maximizing either the far field scattering or the near field enhancement (Figure 1.3). From the results of this work it was concluded that in both configurations MDM structures are advantageous over their solid monometallic counterparts. However, the configuration maximizing the far field scattering would be most beneficial due to the high scattering produced by the FR in the MDM nanoparticles. Spectrally, the Fano resonance features a region of preferential forward and backward scattering, where the monometallic would otherwise only have backward scattering. The backward scattering effects are mitigated because the scattering near the Fano minimum are already small. Meanwhile, the forward scattering effects are exaggerated because the light would preferentially scatter forward. The angle of the scattering of the light offers a good amount of scattering past the critical angle of at which light would be permanently trapped. Furthermore, the

particles can be tuned to cover a broad range of the solar spectrum. Finally, it should be noted that all the simulations have been performed for nanoparticles inside a homogeneous medium. The MDM structures at the interface air-dielectric will have a considerable improvement in the forward scattering. Likewise, when they are embedded inside the near field enhancement will be considerably larger. Hence, the results presented in this work should be interpreted only as a lower limit of what can be achieved.

5.1: Future work

In such a new and promising field, there is much work to be done. The computational work in this paper should be complemented by experimental validation of the observed behavior and mechanisms. A more objective measure of comparing the benefits of far field versus near field effects in increasing solar cell efficiency should be developed.

The possibility and combinations of nanoparticles in plasmonic solar cells is virtually limitless. Au_xAg_{1-x} and double concentric metal systems are all promising. The existing material system could be improved by instead using a silver core, which reaches the LSPR conditions better than gold. The LSPR of gold could also be enhanced by a stronger dielectric layer, either replacing the silica layer or even adding an insulating layer to the current outer metal shell. Outside of the field of photovoltaics, the results could be useful in understanding the plasmonic mechanisms utilized in other fields of biology, chemistry, and physics.

List of References

[1] A. Willoughby and G. J. Conibeer, *Solar Cell Materials, Developing Technologies*, 1 ed., 2014.

[2] Adolf Goetzberger, Christopher Heblinga, and H.-W. Schock, "Photovoltaic materials, history, status and outlook," *Materials Science & Engineering R,* vol. 40, pp. 1-46, 2003.

[3] K. O. Kasap, *Principles of Electronic Materials and Devices*, 3rd ed.: McGraw Hill Education, 2006.

[4] D. S. Philipps and W. Warmuth, "Fraunhofer ISE: Photovoltaics Report," ed. Freiburg, Germany: Fraunhofer Institute for Solar Energy Systems ISE, 2016.

[5] K. R. C. A. Polman, "Plasmonic solar cells," *OPTICS EXPRESS,* vol. 16, 22 December 2008 2008.

[6] L. Solymar, D. Walsh, and R. R. A. Syms, *Electrical Properties of Materials*: Oxford University Press, 2014.

[7] L. Montano-Priede, O. Pena-Rodriguez, A. Rivera, A. Guerrero-Martinez, and U. Pal, "Optimizing the electric field around solid and core-shell alloy nanostructures for near-field applications," *Nanoscale,* vol. 8, pp. 14836-45, Aug 21 2016.

[8] C. F. BOHREN and D. R. HUFFMAN, *Absorption and Scattering of Light by Small Particles*: Wiley VCH, 1998.

[9] J. Mertz, "Radiative absorption, fluorescence, and scattering of a classical dipole near a lossless interface: a unified description," *Optical Society of America,* vol. 17, 2000.

[10] H. A. Atwater and A. Polman, "Plasmonics for improved photovoltaic devices," *Nat Mater,* vol. 9, pp. 205-13, Mar 2010.

[11] U. Fano, "Effects of Configuration Interaction on Intensities and Phase Shifts," *Physical Review,* vol. 124, pp. 1866-1878, 1961.

[12] B. Luk'yanchuk, N. I. Zheludev, S. A. Maier, N. J. Halas, P. Nordlander, H. Giessen*, et al.*, "The Fano resonance in plasmonic nanostructures and metamaterials," *Nat Mater,* vol. 9, pp. 707-15, Sep 2010.

[13] B. G. O. J. F. Martin, "Influence of Electromagnetic Interactions on the Line Shape of Plasmonic Fano Resonances," *American Chemical Society (ACS) Nano,* vol. 5, 2011.

[14] E. Prodan, C. Radloff, N. J. Halas, and P. Nordlander, "A Hybridization Model for the Plasmon Response of Complex Nanostructures," *Science,* vol. 302, pp. 419-422, 2003.

[15] S. Mukherjee, H. Sobhani, J. B. Lassiter, R. Bardhan, P. Nordlander, and N. J. Halas, "Fanoshells: nanoparticles with built-in Fano resonances," *Nano Lett,* vol. 10, pp. 2694-701, Jul 14 2010.

[16] O. Pena-Rodriguez, A. Rivera, M. Campoy-Quiles, and U. Pal, "Tunable Fano resonance in symmetric multilayered gold nanoshells," *Nanoscale,* vol. 5, pp. 209-16, Jan 7 2013.

[17] W. Yang, "Improved recursive algorithm for light scattering by a multilayered sphere," *APPLIED OPTICS,* vol. 42, 2003.

[18] O. Peña and U. Pal, "Scattering of electromagnetic radiation by a multilayered sphere," *Computer Physics Communications,* vol. 180, pp. 2348-2354, 2009.

[19] H. R. Stuart and D. G. Hall, "Absorption enhancement in silicon-on-insulator waveguides using metal island films," *Applied Physics Letters,* vol. 69, p. 2327, 1996.

[20] P. Mandal and S. Sharma, "Progress in plasmonic solar cell efficiency improvement: A status review," *Renewable and Sustainable Energy Reviews,* vol. 65, pp. 537-552, 2016.

[21] Konstatin Ladutenko, Umapada Pal , Antonio Rivera, and O. Y. P. Rodríguez, "Mie calculation of electromagnetic near-field for a multilayered sphere," *Computer Physics Communications,* p. Under Revision, 2016.

[22] C. L. O. Pluchery, *Gold Nanoparticles for Physics, Chemistry and Biology*: Imperial College Press, 2012.

[23] K. M. Mayer and J. H. Hafner, "Localized surface plasmon resonance sensors," *Chem Rev,* vol. 111, pp. 3828-57, Jun 8 2011.

[24] Y. S. No, J. H. Choi, H. S. Ee, M. S. Hwang, K. Y. Jeong, E. K. Lee*, et al.*, "A double-strip plasmonic waveguide coupled to an electrically driven nanowire LED," *Nano Lett,* vol. 13, pp. 772-6, Feb 13 2013.

[25] C. H. Lee, S. C. Liao, T. R. Lin, S. H. Wang, D. Y. Lai, P. K. Chiu*, et al.*, "Boosted photocatalytic efficiency through plasmonic field confinement with bowtie and diabolo nanostructures under LED irradiation," *Opt Express,* vol. 24, pp. 17541-52, Aug 8 2016.

[26] T. Markvart and L. Castañer, "Principles of Solar Cell Operation," pp. 3-25, 2013.

[27] W. Shockley and H. J. Queisser, "Detailed Balance Limit of Efficiency of p-n Junction Solar Cells," *Journal of Applied Physics,* vol. 32, p. 510, 1961.

[28] C. H. Henry, "Limiting efficiencies of ideal single and multiple energy gap terrestrial solar cells," *Journal of Applied Physics,* vol. 51, p. 4494, 1980.

[29] O. Peña-Rodríguez and U. Pal, "Exploiting the Tunable Optical Response of Metallic Nanoshells," in *UV-VIS and Photoluminescence Spectroscopy for Nanomaterials Characterization*. vol. 2, ed, 2013, pp. 99-149.

[30] G. v. Rossum, "Python Tutorial," vol. CS-R9526., ed: CWI Report, May 1995, p. Available at: http://python.org.

[31] P. B. Johnson and R. W. Christy, "Optical Constants of Noble Metals," *Physical Review B,* vol. 6, 1972.

[32] S. S.A. Optical Data from Sopra SA [Online]. Available: http://sspectra.com/sopra.html

[33] C. E. Roman-Velazquez and C. Noguez, "Designing the plasmonic response of shell nanoparticles: spectral representation," *J Chem Phys,* vol. 134, p. 044116, Jan 28 2011.

[34] F. Wooten, *Optical Properties of Solids*, 2 ed. New York City: Academic Press, 1972.

[35] M. V. F. Bashevoy, V. A.

Zheludev, N. I. , "Optical whirlpool on an absorbing metallic nanoparticle," *OPTICS EXPRESS,* 2005.

[36] A. Mejdoubi, M. Malki, M. Essone Mezeme, Z. Sekkat, M. Bousmina, and C. Brosseau, "Optical scattering and electric field enhancement from core–shell plasmonic nanostructures," *Journal of Applied Physics,* vol. 110, p. 103105, 2011.

[37] J. Zuloaga and P. Nordlander, "On the energy shift between near-field and far-field peak intensities in localized plasmon systems," *Nano Lett,* vol. 11, pp. 1280-3, Mar 9 2011.

Appendix A

Table A.1: Line fitting parameters for $t_1 + t_2 = 50$

	t_2					
Parameter	10	15	20	25	30	35
a	2.46	2.50	2.32	3.63	-	-
b	1.67	1.22	0.78	0.50	-	-
q	-0.58	-1.10	-0.97	0.29	-	-
E_a	1.47	1.70	1.86	2.16	-	-
Γ_a	0.11	0.09	0.11	0.16	-	-
E_s	2.09	2.12	2.11	1.89	-	-
Γ_s	0.30	0.27	0.33	0.18	-	-

Table A.2: Line fitting parameters for $t_1 + t_3 = 60$.

	t_1					
Parameter	45	40	35	30	25	20
a	-	2.28	2.50	2.70	2.75	2.53
b	-	1.87	1.22	0.57	0.40	0.65
q	-	-1.06	-1.10	-0.83	-0.37	-0.18
E_a	-	1.55	1.70	1.85	1.99	2.08
Γ_a	-	0.08	0.09	0.10	0.10	0.09
E_s	-	2.11	2.12	2.10	2.07	2.06
Γ_s	-	0.32	0.27	0.26	0.27	0.31